UNIVERSITY OF CALIFORNIA,
IRVINE

Acoustically Enhanced Colloid Transport In Saturated Porous Media

THESIS

submitted in partial satisfaction of the requirements for the degree of

MASTER OF SCIENCE

in Civil Engineering

by

John Matthew Thomas

Thesis Committee:
Professor Constantinos V. Chrysikopoulos, Chair
Professor Brett F. Sanders
Professor Stanley B. Grant

2005

The thesis of John Matthew Thomas is approved:

Committee Chair

University of California, Irvine

2005

Dedication

To all the precious souls who have had a hand in getting me here and making me who I am.

"The heights by great men reached and kept
were not attained by sudden flight,
but they while their companions slept,
were toiling upward in the night!"

-Longfellow

Thanks to Henry Wadsworth Longfellow for this simple thought. It kept me up and toiling through many late nights!

Contents

List of Tables

List of Figures

Nomenclature

a	dummy variable.
A	cross-sectional area of column, [L^2].
$\mathcal{A}$	defined in (4.7).
b	dummy variable.
$\mathcal{B}$	defined in (4.8).
c	dummy variable.
C	concentration of colloids in suspension, [M/L^3].
C^*	mass of colloids adsorbed, [M/M].
d	dummy variable.
D	hydrodynamic dispersion coefficient, [L^2/t].
D_e	effective hydrodynamic dispersion coefficient, [L^2/t].
D^*	component of dispersion attributed to acoustics, [L^2/t].
$\mathcal{D}$	molecular diffusion coefficient, [L^2/t].
$\mathcal{D}_e$	effective molecular diffusion coefficient, [L^2/t].
f	arbitrary function.
h	dummy variable.
$\mathcal{H}$	defined in (4.9).
J_0	Bessel function of zero order, [-].
J_1	Bessel function of first order, [-].
k_c	forward rate coefficient, [1/t].
k_r	reverse rate coefficient, [$M/L^3/t$].
l	dummy variable.

L column length, [cm].

$\mathcal{L}$ Laplace transform, [-].

$\mathcal{L}^{-1}$ inverse Laplace transform, [-].

M defined in (4.22).

M_0 mass injected over cross-section of column, [M/L^2].

M_{beads} mass of glass beads in column, [M].

M_{inj} mass injected, [M].

N defined in (4.22).

P_1 influent acoustic pressure, [kPa].

P_2 effluent acoustic pressure, [kPa].

ΔP acoustic pressure gradient, [kPa/cm].

q seepage velocity, [L/t].

Q volumetric flow rate, [L^3/t].

r_1 forward rate coefficient, [1/t].

r_2 reverse rate coefficient, [M/L^3/t].

s Laplace time variable, [-].

t time, [t].

u dummy variable.

U average interstitial fluid velocity, [L/t].

U_e effective interstitial fluid velocity, [L/t].

U^* component of velocity attributed to acoustics, [L/t].

V_{beads} volume of beads, [L^3].

V_{total} total volume of solid matrix, [L^3].

V_{voids} volume of void space, [L^3].

x longitudinal spatial coordinate, [L].

Greek Letters

α_1 dummy variable.

α_2 dummy variable.

α_L longitudinal dispersivity, [L].

γ Laplace space variable, [-].

δ Dirac delta function, [1/t].

ζ dummy integration variable.

θ porosity (void volume/total volume), [L^3/L^3].

Θ defined in (4.34).

λ inactivation constant of suspended colloids, [t^{-1}].

λ^* inactivation constant of adsorbed colloids, [t^{-1}].

π constant, [-].

ρ bulk density of the solid matrix, [M/L^3].

τ dummy integration variable.

τ^* tortuosity, [-].

Φ defined in (4.49).

Ω defined in (4.58).

Acknowledgments

First and foremost, at the risk of sounding "cliché", I want to thank my God for getting me through some of the most emotionally and physically draining ordeals of my life, which just happened to coincide with my first years of graduate study. There is no doubt in my mind that without your strength I could not have done it. A special thanks to my professor Dr. Costas Chrysikopoulos who gave me the necessary guidance and prodding to finish. Your patience is greatly appreciated. Thanks to Dr. Eric Vogler who was of invaluable help in the laboratory and in learning the ropes of university politics. Thanks to Drs. Brett Sanders and Stanley Grant for serving on my committee and for many thought provoking and insightful conversations that helped me along the way. Thanks to Steve Bowen who convinced me not only that I could, but also that I should go to graduate school. Thanks to Cecily Storey for your expert help with laboratory experiments. Thanks to my officemates Richard Argall, Julio Fernandez, and Robert Mrse, all of whom both encouraged me and shared in the pain. There's just something about knowing that you're not the "only one". Thanks to my family and many friends who stood by me and supported me through all the difficult times. Without all of you, I quite literally would not have made it. I believe myself to be a product of the individuals whose lives I have been priveledged to be a part of and, as such, you all share in any accomplishments I might claim. The value of your love, compassion, encouragement, advice, and admonishment cannot be overstated. My sincerest thanks! Thanks to the Department of Civil and Environmental Engineering at UCI, the National Science Foundation, and the Fariborz Maseeh Fellowship for the financial support that allowed me to finish this work.

Finally, thank you my Lord and Savior Jesus Christ. You have always reminded me that despite how easily I can become consumed with my work, in the end none of this really matters. I am but a stranger here, my home and citizenship is elsewhere. Thanks for walking with me through this Odyssey called life, and especially at those times when you were my only companion.

Abstract of The Thesis

Acoustically Enhanced Colloid Transport In Saturated Porous Media

by

John Matthew Thomas

Master of Science in Civil Engineering

University of California, Irvine, 2005

Professor Constantinos V. Chrysikopoulos, Chair

The effects of acoustic wave propagation in the direction of flow on the transport of colloids in saturated porous media was investigated by injecting a multicomponent tracer pulse into a glass-bead-packed column with a background flow and an acoustic source connected on the influent end. Acoustic pressure at the influent was maintained at 23.0 kPa. Experiments were conducted at acoustic frequencies of 30, 50, 70, 90, 110, 130, and 150 Hz. The fitted hydrodynamic dispersion for the case of no acoustic pressure (base case) for Uranine (molecular solute), and blue and red polystyrene microspheres (colloids of diameter 0.10 μm and 0.028 μm) was 5.35, 7.07, and 7.12 cm^2/h, respectively. The fitted values of the forward and reverse rate constants, r_1 and r_2, were 5.38×10^{-2} h^{-1} and 2.49 h^{-1} for blue microspheres, and 5.31×10^{-2} h^{-1} and 2.51 h^{-1} for red microspheres. Acoustic pressure forcing caused an increase in effective interstitial velocity at all frequencies for the conservative tracer and colloids of both size. The maximum increase in velocity occurred at 70 Hz. Acoustics also caused increased dispersion above the base case at all experimental frequecies. There was a very large observed spike in dispersion at 30 Hz. For

the range of experimental frequencies, applied acoustic pressure increases the rate of colloid transport and dispersion in saturated porous media. The exact mechanisms for this are still under investigation.

Chapter 1

INTRODUCTION

1.1 Significance of Research

Groundwater contamination by various pollutants is a major concern in both developed and developing nations. Groundwater aquifers are often contaminated by an assortment of pollutants that derive from various sources. One common class of groundwater contaminant is dissolved molecular solutes. Examples include pesticides and fertilizers from agricultural runoff, nitrate and nitrite from wastewater release, and perchlorate, which was commonly used in the manufacture of rocket fuels and ballistic weaponry in the past. Another common class of groundwater pollutants is colloidal particles such as viruses and bacteria (biocolloids) from domestic or industrial wastewater spills and radionuclides that can leach into groundwater from deep geological disposal sites. A third common class of pollutant is dissolved light or dense non-aqueous phase liquids (NAPLs) such as TCE, PCE, and gasoline by-products from leaking storage tanks, leaking pipelines, or accidental spills [*Gross et al.*, 2003; *Chrysikopoulos et al.*, 2002; *Bao et al.*, 2003; *Tien and Li*, 2002].

Adverse health effects in humans and animals caused by these contaminants are well documented. In many parts of the world, including the United States, groundwater is a primary drinking water source; it is pumped and distributed directly into homes

for consumption without any treatment. Due to epidemiological concerns of these potential hazards their subsurface fate and transport have been receiving interest in water resources research for some time. For example, in 1993, McCarthy and Wobber reported that the movement of pathogenic bacteria, protozoa, and viruses through the subsurface had, at that time, already long been a topic of research because contamination of water-supply wells by microbial pathogens contributes substantially to waterborne disease outbreaks. This is certainly true in developed nations and may be of particular concern in developing nations where environmental laws and practices to mitigate potential hazards to human health are lacking. Thus remediation of contaminated groundwater aquifers is a truly global problem.

In the United States and other developed nations, strict environmental laws passed over the past four decades have facilitated changes in manufacturing and disposal techniques and interest in groundwater remediation methods for these types of contaminants. Success in the elimination and remediation of contaminants is dependent upon understanding the major pathways and mechanisms of contaminant transport. While a great deal of research has been done on the subject, currently employed technologies fall into a few categories.

1.2 Conventional Remediation Methods

There are a number of available technologies for treatment of contaminated groundwater that have been utilized with varying degrees of success. The most commonly used technologies are filtration through granular activated carbon (GAC), soil removal and/or washing, air stripping, and biological contact or trickle filtration. Regardless of the technology used, once the water is treated it is either disposed of on the surface or re-injected into the groundwater aquifer.

1.2.1 Pump-and-Treat Methods

The aforementioned remediation technologies rely heavily on pump-and-treat methodology; contaminated water is pumped to the surface and treated there. In general then, the amount of contaminant mass removed is a function of the amount of water pumped from the subsurface and the concentration of dissolved or suspended contaminant in that water. For this reason groundwater remediation is energy-intensive and costly, especially in places where the groundwater table is deep. However, the greater the partitioning of the contaminant from solid or liquid to aqueous phase, the faster and less costly is remediation. Therefore remediation is limited by the aqueous solubility of the contaminant. Unfortunately, several of these contaminants have low aqueous solubilities (e.g., DNAPLs [*Vogler and Chrysikopoulos*, 2001]), or high affinities for adsorption to the porous media. Figure 1.1 demonstrates how these contaminants persist once they have entered the aquifer.

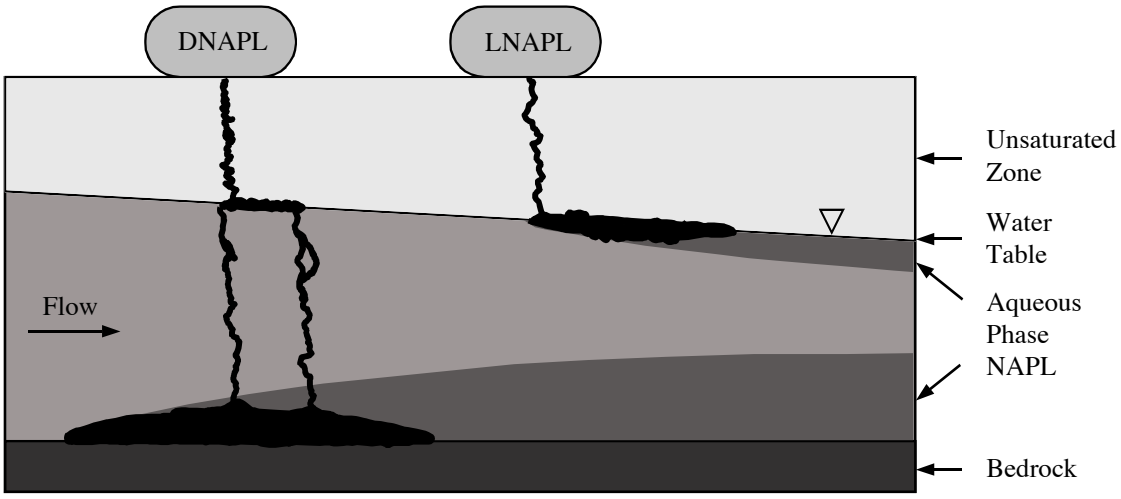

Figure 1.1: DNAPLs and LNAPLs form pools in the aquifer and then slowly dissolve into flowing groundwater creating a lasting contamination source.

DNAPLs are denser than water and therefore migrate downward through the soil creating a pool when they reach an impermeable zone such as bedrock. LNAPLs are less dense than water and therefore create a floating pool on top of the water table.

Both LNAPL and DNAPL pools slowly dissolve into flowing ground water creating a long persisting source of contamination. Their low aqueous solubility and persistence in the subsurface make the achievement of complete reclamation impossible in most cases [*Gross et al.*, 2003].

1.2.2 Alternative Methods

Various methods of contaminant transport enhancement in porous media have been explored extensively in recent years by environmental engineers and scientists who design remediation methods for contaminated subsurface formations [*Vogler and Chrysikopoulos*, 2002]. Most of these in-situ methods involve introduction of non-indigenous colloids or humic substances, specialized biocolloids, surfactants, or co-solvents to optimize contaminant scavenging, reduce permeability of a formation, or enhance bioremediation. All these substances are considered to be either contaminants themselves or undesirable in drinking water supply.

1.3 Research Objectives

An important direction for water resources research is a clean technology that will increase contaminant mass transport in porous media with conventional pump and treat methods, thereby facilitating enhanced remediation, without adding further contaminants to the subsurface. An example of such a clean technology is the introduction of acoustic (sound) waves in saturated porous media to increase contaminant mass transport. More contaminant mass in the volume of water removed means more remediation for the dollar. The literature shows that acoustic waves can increase the effective interstitial velocity and thus breakthrough time of conservative tracers in packed column experiments and can increase the dissolution of DNAPLs in water [*Vogler and Chrysikopoulos*, 2002, 2004; *Chrysikopoulos and Vogler*, 2004]. It should be noted that the physical processes responsible for these observations have not been

sufficiently defined or developed.

This work is an experimental investigation of the effects of acoustic waves on the transport of colloids in porous media. The critical importance of colloids in groundwater systems and their implications for contaminant transport will be discussed in the literature review. The objectives of this research are to explore whether acoustic waves enhance colloid transport in porous media and to quantify the effects of various acoustic frequencies with a constant acoustic pressure on colloid transport. To my knowledge, no one has studied the effects of acoustic waves on the transport of colloids.

Chapter 2

LITERATURE REVIEW

2.1 Acoustic Wave Propagation

Wave propagation in porous media is of interest in various diversified areas of science and engineering. The theory of the phenomenon has been studied extensively in soil mechanics, seismology, earthquake engineering, ocean engineering, geophysics, and many other disciplines [*Corapcioglu and Bear*, 1991]. However, only recently has the concept of using waves for aquifer remediation been given attention. Gross et al., 2003, have suggested that the unique significance of introducing pressure waves (a type of wave including acoustic waves) into an aquifer as well as its economic potential is in the ability to focus on cleaning groundwater at localized sites, mobilize trapped contaminants, and guide the motion of a contaminant plume by controlling the intensity and direction of the applied pressure.

2.1.1 Wave Propagation In Saturated Porous Media

Acoustics is a general term referring to time-varying deformations or vibrations in materials. When the particles of a medium are displaced from their equilibrium positions, while remaining within the elastic limit of the medium, internal (electro-

static) restoration forces and inertia of the particles lead to oscillatory motion of the medium. The atoms in the material move in unison to produce a mechanical wave.

Acoustic waves (pressure waves in the audible frequency range) can propagate as longitudinal waves, shear waves, surface waves, and in thin materials, as plate waves. The waves of interest in saturated porous media are longitudinal and shear waves. In longitudinal waves, the oscillations occur in the longitudinal direction or the direction of wave propagation. Since compression and dilation forces are active in these waves, they are also called pressure or compression waves. Compression waves can be generated in liquids as well as solids because the energy travels through the atomic structure by a series of compression and expansion (rarefaction) movements. In the transverse or shear wave, the particles oscillate at a right angle or transverse to the direction of propagation. Shear waves require an acoustically solid material for effective propagation and, therefore, are not effectively propagated in materials such as liquids or gasses. Shear waves are relatively weak when compared to longitudinal waves.

Porous media is viewed as a continuum consisting of a solid phase (either compressible or incompressible) and one or more fluids (gases and liquids). The solid phase constitutes the solid matrix with interconnected void space filled by fluids. Both longitudinal and shear waves propagate in the solid phase and longitudinal waves only in the liquid phase. The speed of a wave traveling within the solid or liquid phase is a function of the material properties of the solid or liquid and is therefore different in each. Wave speed is also independent of the amplitude of the sound wave. Stress-strain relations for the medium are generally expressed in terms of elastic constants of the solid and fluid phases. Biot, 1956a,b, was the first to introduce these relations into the conservation of linear momentum and solid and fluid mass balance equations. Thus he mathematically described the process of wave propagation in porous media. The solutions to his equations give the velocity of the waves traveling through the media. This is useful in some applications such as seismology, but not particularly for remediation. The important consideration for remediation is how

acoustic waves affect fluid dynamics on the pore scale and how they affect transport and dissolution.

2.1.2 Effects of Acoustics on Pore Fluid

Acoustics have a profound affect on the hydrodynamic processes within individual pores. The general phenomena of oscillatory forcing (e.g., application of acoustic waves) in porous media may have a dramatic effect on the flow resistance or mean flow rate in pressure-driven flows through porous media. One of the distinct features of oscillatory forcing is that it is possible to reach significant pore-scale Reynolds numbers in porous media where such Reynolds numbers would be impossible to achieve in a steady pressure-driven flow [*Graham and Higdon*, 2002]. At these high Reynolds numbers a number of non-linear flow regimes may exist. Graham and Higdon, 2002, identified three nonlinear phenomena that may lead to enhanced transport in the presence of oscillatory driving forces: nonlinear dependence of flow rate on driving force, existence of multiple solutions with different flow rates at the same forcing level, and anisotropy arising in certain geometries at finite Reynolds numbers. It should be noted that Graham and Higdon concluded that the final disposition of the flow depends on the influence of the unsteady inertial terms in the time-dependent Navier-Stokes equations. Lab and field tests have also shown that acoustic stimulation can increase the effective permeability of the porous medium resulting in higher flow rates for a given pressure drop [*Beresnev and Johnson*, 1994].

2.1.3 Effects of Acoustics on Solute Transport

Several studies have shown that acoustic waves can increase solute mobilization in saturated porous media. For example, acoustic waves were found to enhance transport of a conservative tracer in packed column experiments with the effective velocity of the solute being approximately inversely proportional to the frequency of the acoustic wave [*Vogler and Chrysikopoulos*, 2002]. Other experimental results have

also shown that significant displacement of solute in saturated porous media results from the propagation of pulsed compression waves [*Gross et al.*, 2003]. A similar effect was demonstrated using shockwaves and other types of pressure waves with conservative tracers. It should be noted that the governing mechanisms responsible for the enhanced transport phenomenon are still under investigation.

2.1.4 Effects of Acoustics on NAPL Ganglia

Experimental evidence also shows that acoustic waves can increase both mobilization and dissolution in multi-phase systems (i.e., oil/water, NAPL/water). Thomas and Narayanan, 2002, showed that mass transfer of a species is enhanced by several orders of magnitude when it is present in a fluid medium that is subject to oscillatory motion, even if there is no net total flow over a cycle of the oscillation. Fieldwork has also shown that the application of acoustic waves can increase oil production from oil-saturated rock. While the exact physical mechanisms for enhanced oil production through acoustic stimulation are unclear, there are several possible mechanisms hypothesized. Acoustic oscillations may act to force a suspended oil droplet through a narrow constriction, to reduce the flow resistance by deforming the droplet or to displace droplets attached to solid surfaces [*Graham and Higdon*, 2002]. Experimental evidence has shown that effluent aqueous DNAPL concentration increased with the application of acoustic pressure waves with the greatest dissolution enhancement occurring at lower frequencies. Furthermore, ganglia mobilization occurred at lower background pressure-driven flow rates with acoustic pressure added [*Chrysikopoulos and Vogler*, 2004].

2.1.5 Effects of Acoustics on Colloid Transport

The effects of acoustic waves on colloid transport in saturated porous media have not yet been studied.

2.2 Physicochemical Characteristics of Colloids

In general, colloid transport in the subsurface is a function of hydraulic factors, geological structure, and interactions between the surfaces of colloids and porous media. These in turn are the result of the physical structure and surface chemistry of the colloids as well as the chemistry of the groundwater and the physical and chemical nature of the porous media.

2.2.1 Physical Structure of Colloids

Colloids represent a class of very fine particles that have some linear dimension between 1 and 1000 nanometers [*Stumm*, 1993; *Chrysikopoulos and Sim*, 1996]. The particle dimension rather than chemical composition, source, or physical state (phase), designates it a colloid [*Hiemenz and Rajagopalan*, 1997]. Colloids are ubiquitous in groundwater aquifers. Typical colloids present in groundwater include clay minerals, oxides or hydroxides of Fe and Al, colloidal silica, organic matter such as humic macromolecules, and biocolloids such as viruses and bacteria [*Kretzschmar and Sticher*, 1998; *Tatalovich et al.*, 2000; *Chrysikopoulos and Abdel-Salam*, 1997]. An important result of their small size is that they tend to remain suspended in solution due to Brownian motion: the random motion of molecules. Colloidal particles will remain in suspension unless they aggregate to form larger particles that can settle due to gravity or they adhere to surfaces of larger particles [*McCarthy and Wobber*, 1993]. There are two important consequences of the size range of colloids: colloidal materials have enormous surface areas and surface energies, and the properties of colloidal particles are not always those of the corresponding bulk matter or those of the corresponding atoms or molecules [*Hiemenz and Rajagopalan*, 1997]. The result is that in addition to physical structure, surface chemistry becomes extremely important in colloid interactions.

2.2.2 Surface Chemistry

The increasing importance of the surface area as the linear dimensions of particles decrease can be understood by considering a quantity known as the specific surface area, A_{sp}, of a substance. This quantity is determined as the ratio of the area divided by the mass of an array of particles as

$$A_{sp} = \frac{A_{tot}}{m_{tot}} \tag{2.1}$$

For spherical particles equation (2.1) becomes

$$A_{sp} = \frac{3}{\rho R_s} \tag{2.2}$$

where ρ is the density of the particle and R_s is the particle radius. From the equation (2.2) it can be seen that as the particle radius, and hence the size of the particle decrease, a larger number of atoms in the particle become surface atoms. The result is that relatively weak forces such as van der Waals forces, electric double layer forces, and electrostatic forces have a profound affect on colloid transport and deposition and their ability to mobilize other contaminants.

2.3 Transport and Deposition of Colloids

The mobilization, transport, deposition, and release of colloidal particles in natural subsurface porous media have received a great deal of attention in the past decade. Their understanding is important for many subsurface applications: to assess contamination potential and protect drinking water supplies from mobile pathogenic microorganisms or radionuclides, to develop engineered bioagumentation and bioremediation strategies, and to quantitatively predict colloid-facilitated transport of many organic and inorganic contaminants [*Bradford et al.*, 2003; *Camesano et al.*, 1999; *Sirivithayapakorn and Keller*, 2003].

The transport of colloids through porous media strongly depends on the kinetics of colloid deposition and release [*Kretzschmar and Sticher*, 1998]. A good synopsis of

the development of transport and deposition models for colloids has been provided by Loveland et al., 2003: "Initially, colloid transport models portrayed the attachment of colloids (and "biocolloids") to porous media as equilibrium sorption. Later, colloid filtration (irreversible first-order attachment) was introduced in conjunction with equilibrium sorption in two-site models. In most cases, colloid transport in homogeneous porous media was adequately characterized by first order attachment and release." For example, Sim and Chrysikopoulos, 1995, presented models of biocolloid (virus) transport with first order attachment, release, and inactivation for the case of linear reversible sorption equilibrium and nonequilibrium adsorption. Loveland goes on to say that further advances have focused on the dynamics of particle deposition (blocking and ripening), the geochemical heterogeneity of aquifer grain surfaces, and the physical heterogeneity of the porous medium.

Deposition of colloids in the subsurface involves several interrelated processes such as aggregation, straining or collision filtration, and settling. As has been discussed, the factors affecting these processes are physical structure of colloids such as colloid density, size, and shape; and surface chemistry, especially specific area. Other important processes that affect colloid transport and deposition in groundwater are solution chemistry, especially pH and ionic strength; and properties of the porous media such as size exclusion effects that lead to increased interstitial velocity, and surface charges [*Kretzschmar and Sticher*, 1998; *McCarthy and Zachara*, 1989; *OMelia et al.*, 1997; *Sirivithayapakorn and Keller*, 2003].

2.3.1 Solution Chemistry

Solution chemistry is important in colloid mobilization because of its ability to affect the weak surface interactions that have been previously mentioned: van der Waals forces, electric double layer forces, and electrostatic forces. For example, increasing the charge development by pH manipulation of the solution can promote detachment and mobilization of colloids. Likewise, colloids such as clays may be immobilized

through van der Waals attractions that exceed electrostatic repulsions, reduced by narrow, diffuse double layers. McCarthy and Wobber, 1993, reported that if subsurface ionic strength were lowered with the concomitant expansion of double-layer thicknesses around the clays, these aluminosilicate colloids could be dispersed into the flowing groundwater.

2.3.2 Physicochemical Properties of Porous Media

One of the most interesting properties of colloids in subsurface systems is that mobile colloids can be transported through natural porous media at a greater velocity than conservative solute tracers. Abundant experimental evidence shows that in column experiments, colloids can have a faster breakthrough compared to solute tracers (e.g. [*Champ and Schroeter*, 1988; *Enfield et al.*, 1989; *Kretzschmar and Sticher*, 1998; *Niehren and Kenzelbach*, 1998]). It is also widely accepted that colloids arrive earlier in the effluent than a nonsorbing conservative tracer in well-characterized natural fractures [*Reimus et al.*, 1995]. This is a direct result of the physicochemical properties of both the colloids and the porous media.

There are a number of ways this early breakthrough effect is explained in the literature. Grindrod et al., 1996, explained that in natural porous media there exist zones of low-permeability. Colloids are either physically excluded from low-permeability zones or are entrapped there physically or chemically. In general, these low-permeability zones are saturated and may still allow solute tracers into them. Others have explained this as a size exclusion chromatographic effect where colloids are physically excluded from small pore spaces where conservative tracers can diffuse [*Kretzschmar and Sticher*, 1998; *Kretzschmar et al.*, 1995; *Enfield et al.*, 1989; *Higgo et al.*, 1993]. These pore spaces are either smaller than the colloids or, if larger, have a constriction in their opening (throat) that is smaller than the colloid so that they are physically excluded. Another way this has been stated is that if colloids are large enough, they do not experience matrix diffusion (diffusion into tiny pores in the

actual media) simply because they are larger than the pores [*Reimus et al.*, 1995]. Still others have shown that because of their large size and low diffusivity they tend to be excluded from regions of low groundwater velocity [*McCarthy and Zachara*, 1989; *Smith and Degueldre*, 1993]. Assuming a no slip boundary condition or zero velocity at all interfaces between water and porous media, this means that colloids can not diffuse into the regions of lowest velocity streamlines. Whatever the physical mechanism, the result is that colloids follow preferential flow paths and may break through before conservative tracers. Whether or not colloids actually experience enhanced mobility depends on the nature of the colloid-matrix interactions (surface chemistry), with unfavorable deposition interactions resulting in enhanced mobility [*Reimus et al.*, 1995], and on the size of the pore spaces in the porous media.

2.4 Colloid-Facilitated Contaminant Transport

In 1988, the U.S. Department of Energy's Subsurface Science Program established a research program that emphasized research on the critical role of colloidal-size particles and biocolloids in facilitating contaminant transport and in remediation. Since then a great deal of research has been done in this area.

There is substantial evidence from both laboratory and field experiments that colloids are efficient sorbents for contaminants such as heavy metals, nonpolar organic compounds, and radionuclides. Transport in groundwater of some contaminants, such as radionuclides, can be facilitated in the presence of colloidal particles (e.g., [*Mill et al.*, 1991; *Corapcioglu and Jiang*, 1993; *McCarthy*, 1998]). This is a direct result of colloid surface chemistry, as was previously discussed, because colloids have a large number of reactive surface functional groups per unit mass (i.e., a high specific area, Asp) [*Kretzschmar and Sticher*, 1998; *Chrysikopoulos and Abdel-Salam*, 1997]. Tatalovich et al., 2000, showed that applying humic substances to groundwater contaminated with a DNAPL pool enhanced the mass transfer of DNAPL to the aqueous phase.

These phenomena become important in groundwater aquifers for contaminant transport and remediation considerations. From the negative viewpoint, some colloids such as bacteria, viruses, and radionuclides, are contaminants themselves, while others such as clay particles and humic substances can increase contamination by acting as mobile sorption sites for other contaminants. Thus these colloids can cause additional contaminant migration. However, because colloids have the ability to increase mass transport of some types of contaminants, this phenomenon can be exploited to enhance remediation techniques. The key from a remediation standpoint is to enhance colloid mass transport in the contaminated porous media while utilizing conventional pump and treat methods. Consequently this has potential to reduce the required pump-and-treat aquifer remediation time.

Chapter 3

EXPERIMENTAL DESIGN AND PROCEDURES

3.1 Physical Description of Apparatus

As has been stated, the objectives of this research are to investigate whether acoustic wave propagation in the direction of flow enhances colloid transport through porous media and to quantify the effects of various frequencies of acoustic pressure oscillation with a constant magnitude of acoustic pressure on colloid transport through porous media. The objectives were accomplished by injecting a multicomponent tracer pulse into the injection port of a 30 cm long glass-bead-packed water-saturated glass laboratory column with a 2.5 cm inner diameter (Kimble Kontes, New Jersey). The injection port was fitted with a stainless steel tube and septum, which allowed the injection needle to penetrate to the center of the glass-bead pack within the column. This allows both the injection point and sampling point to be directly in line in the direction of flow which gives physical justification for the selection of one-dimensional transport in the analytical solution developed in the next chapter. To ensure consistent injections between experiments and thereby reduce experimental error in the measured dispersion of the tracer, a special syringe injector was constructed. The

syringe injector consists of a syringe holder, two steel sliders, a syringe depressor, and springs. The syringe holder keeps the syringe stationary while the depressor is pulled away from the holder stretching the springs. When released the spring force pulls the depressor along the sliders into the syringe plunger and injects the tracer solution. Figure 3.1 is two photographs of the syringe injector before and after injection. The

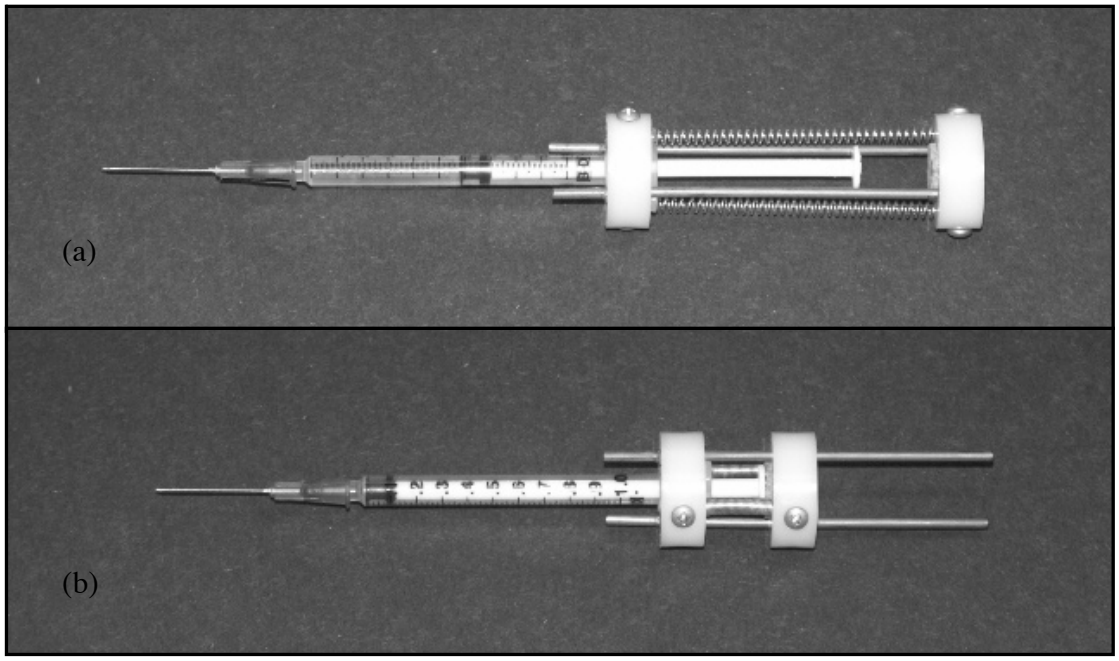

Figure 3.1: (a) A photograph of the syringe injector and syringe ready for injection with springs stretched. (b) A photograph of the syringe injector and syringe after injection with springs relaxed.

column was packed with 2 mm diameter soda-lime glass beads (Fisher Scientific, New Jersey) as a model porous media. Glass beads were chosen as model porous media because they are uniform in size thus creating relatively uniform pore spaces, they are chemically nonreactive with the solutions used in these experiments, and the have a uniform negative surface charge [*Weronski et al.*, 2003]. The beads were retained in the column with teflon screens placed on both the influent and effluent ends of the column. The screens allow water and colloids to enter and exit the bead pack unimpeded as well as allowing acoustic wave propagation from the reservoir through

the column. The teflon screens were held in place by teflon column end caps which in turn were held in place by plastic retainers that screw into threads molded in the ends of the glass column. Figure 3.2 shows how the glass-bead pack is retained in the column while allowing acoustic wave propagation. The teflon end caps were milled to accommodate 1/4 inch stainless steel fittings (Swageloc) for 3/8 inch semi-rigid plastic tubing (Fisher Scientific, Pennsylvania). Both teflon and stainless steel are

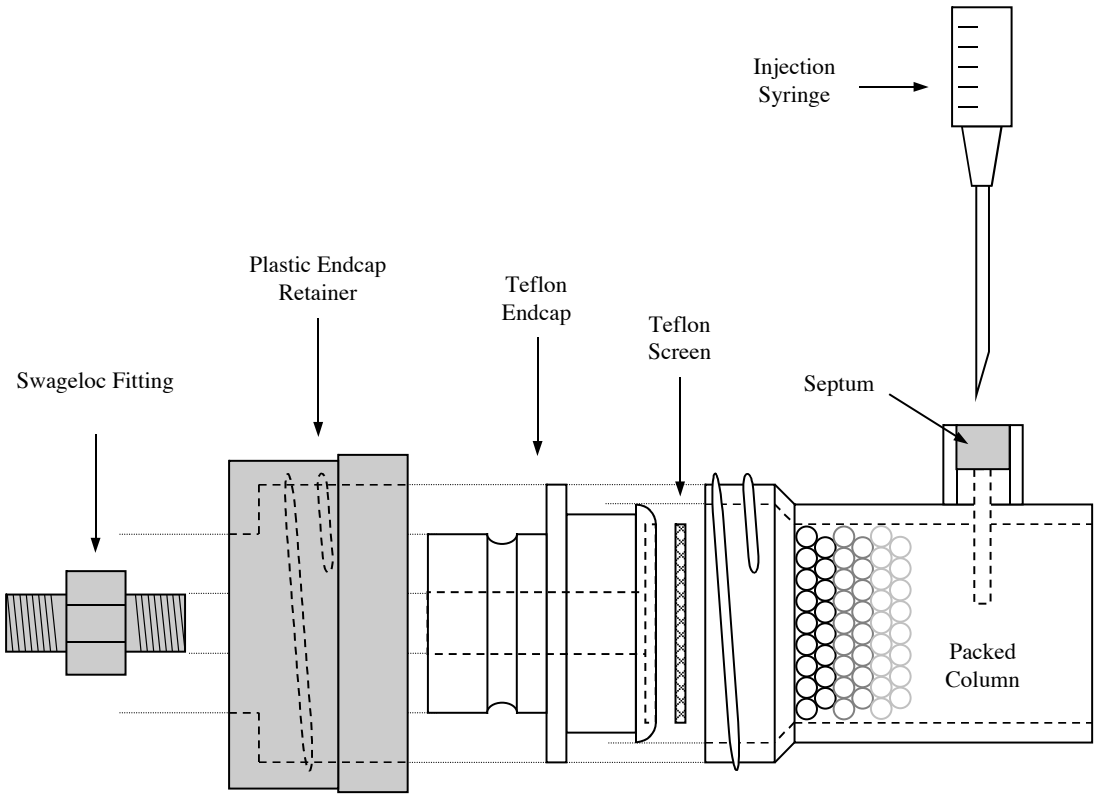

Figure 3.2: A schematic of how the glass-bead pack is retained in the column while allowing acoustic wave propagation.

chemically nonreactive with the solutions used. Constant flow of purified water at a rate of 0.80 mL/min was maintained through the packed column with a dual-syringe infusion pump (KDS200; KD Scientific, Massachusetts). Acoustic pressure waves were introduced into the column by the oscillation of a pressure transducer (TST37; Clark Sythesis, Colorado). The transducer was mounted securely to a laboratory countertop with a bracket specifically designed to limit vibration so that all the

acoustic energy would be transferred to the column. The only physical connection of the transducer to the glass column was through a small plunger. The plunger was attached to the transducer on one end and a neoprene diaphram on the other end. The diaphram was secured to a specially designed reservoir milled out of plexiglass. The reservoir and the column were filled with purified water. Wave propagation through the water and porous media occurred when the diaphram was oscillated by the transducer. The frequency of acoustic pressure oscillation was controlled by a function generator (FG-7002C; LG Precision, California). The magnitude of acoustic pressure was controlled by an amplifier (Lab300; Lab Gruppen, Sweden) and was measured with PCB106b pressure sensors in conjunction with 480E09 ICP sensor signal conditioners (PCB Piezotronics, Inc., New York) and a digital multimeter (MXD-4660A; Metex, Korea). The pressure sensors were mounted on the influent and effluent ends of the glass-bead pack. A complete schematic of the experimental apparatus employed in this study is shown in Figure 3.3. A top-down detail of the encircled area of 3.3 is shown in Figure 3.4. This shows how the transducer, plunger, diaphram, and reservoir are connected for acoustic wave propagation. Effluent samples were collected at regular intervals from a dedicated needle (sampling port) mounted with its sharpened end resting against the teflon screen that retained the glass bead pack on the effluent end of the column. Beyond the sampling port the effluent tube was bent upward and then leveled to create a constant background pressure head.

3.2 Experimental Procedure

Column apparatus and all accessories were carefully cleaned between experiments by pumping several pore volumes of a strong acid (HCl) followed by several pore volumes of purified degassed water, similar to the process performed by Weronski et al., 2003. This procedure ensured that the column and media were free from contaminants and microorganisms and that solution chemistry was uniform between

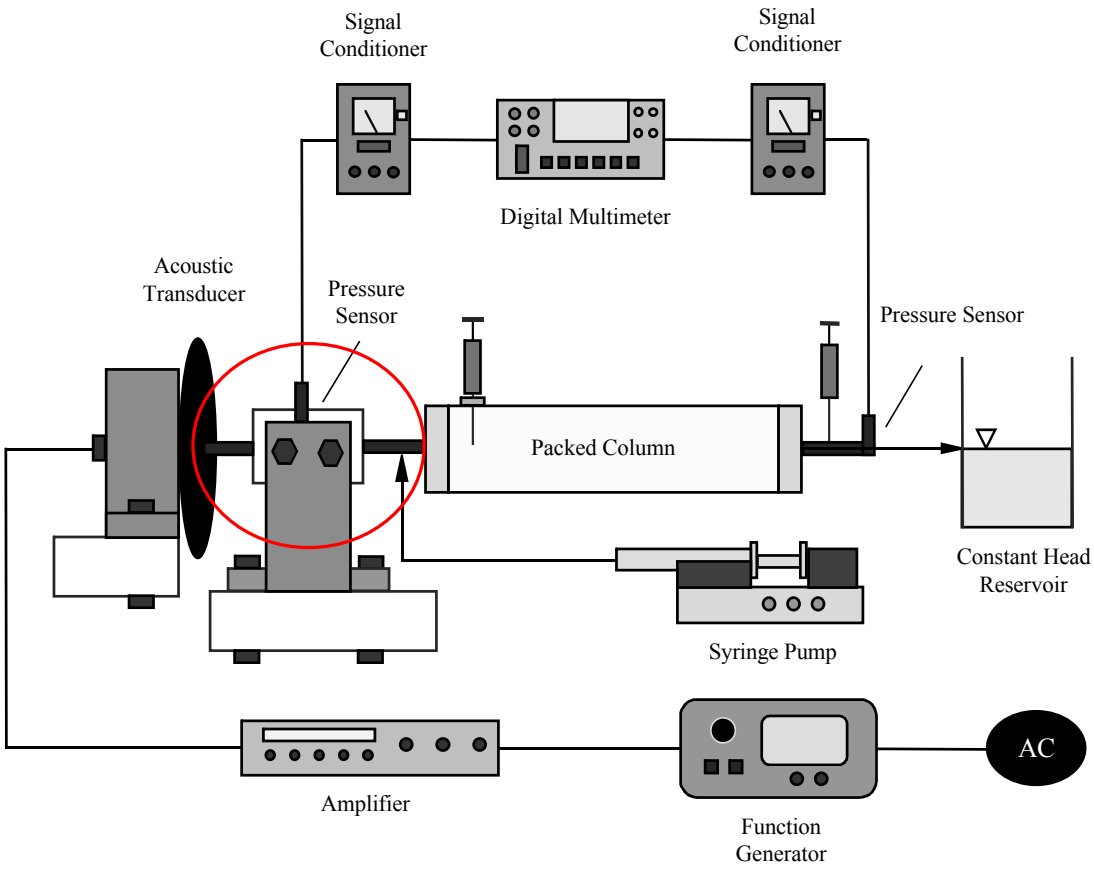

Figure 3.3: The experimental apparatus used in the acoustic experiments described.

experiments. All water used in these experiments was purified with a Milli-Q UV plus water purification system (Millipore Corp., Massachusetts) with a filter size of 0.22 μm and UV sterilization then polished to a specific resistance of 18.2 mΩ-cm. Table 3.1 shows the finished water purity parameters of the water used in these experiments. The water was then vacuum degassed in a clean vacuum flask for at least 15 minutes before being run through the column to remove dissolved gases and to prevent absorption of carbon dioxide (CO_2) gas. Dissolved CO_2 forms carbonic acid and can reduce the pH of the water thereby changing the transport and deposition properties of colloids. Degassing allows the pH of the water throughout these experiments to remain at pH 7.2. The effects of solution chemistry (i.e., pH) on the transport and deposition of colloids has been discussed in Section 2.3.1.

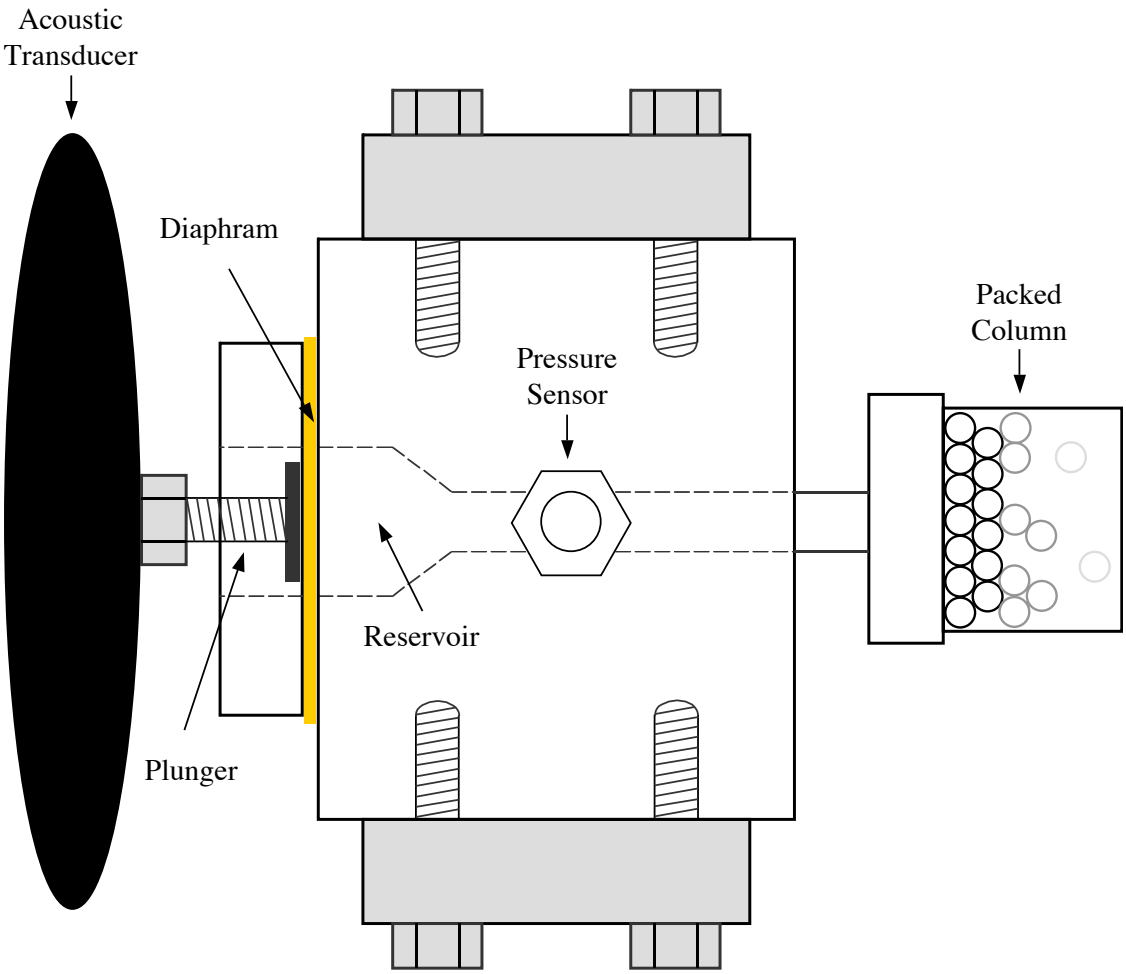

Figure 3.4: A top-down detail of the pressure transducer, plunger, diaphragm, and acoustic reservoir encircled in Figure 3.3

After several pore volumes of purified water were pumped through the column an effluent sample was analyzed for chloride ions using an ion chromatograph (DX120; Dionex, Massachusetts) to ensure that there were no traces of HCl remaining in the column. If any HCl remained, several more pore volumes of purified water were pumped through the column and the effluent tested again until there were no traces of HCl. The multicomponent tracer injected into the column was made prior to each experiment by combining exactly 1.0 mL of a conservative tracer stock solution, 1.0 mL of blue microsphere stock solution, and 1.0 mL of red microsphere stock solution. The conservative tracer stock solution was a 5 mg/L solution of Fluo-

Table 3.1: Water Purity Parameters

Parameter	Specification
Resistivity	18.2 mΩ-cm
Total Organic Carbon	$\leq$ 5 ppb
Particles $\geq$ 0.22 μm	$<$ 1/mL
Total dissolved solids	$<$ 10 ppb
Silicates	$<$ 0.1 ppb
Heavy metals	$\leq$ 0.1 ppb
Microorganisms	$\leq$ 1 cfu/mL

rescein Sodium Salt ($C_{20}H_{10}Na_2O_5$) commonly known as Uranine (Fisher Scientific, New Jersey). The blue and red microsphere stock solutions were one-in-twenty dilutions of commercially available one-percent-by-mass solutions of fluorescent-dyed polystyrene microspheres (Duke Scientific, California) of a specific diameter. The colors (i.e., blue and red) refer to the fluorescent properties of the microspheres and will be discussed in detail in Section 3.3.2. Each color also corresponds to a specific diameter of the particles so that each stock solution contained microspheres of only one specific diameter. The flow rate of the pump was set to 0.80 mL/min and a slug of 0.6 mL of the multi-component tracer solution was instantaneously injected with the syringe injector into the column through the injection port located near the influent end of the column. Elapsed time was measured with a digital quartz chronograph (Timex, New Jersey). Five dilutions of the remaining multicomponent tracer were made in 50 mL volumetric flasks labeled C1 through C5 and a sample of each was transferred to a 1 cm pathlength disposable polyethylene cuvette (Cole Parmer Instrument Co., Illinois). Sample cuvettes were then labeled from 38 minutes to 106 minutes by two-minute increments. Sample effluent volumes of 0.5 mL were collected from the sampling port at regular two-minute intervals beginning at 38 minutes from time of injection using a dedicated disposable 1.0 mL tuburculin plastic

syringe (Becton Dickinson and Co., New Jersey). The samples were then transferred to cuvettes where exactly 1.5 mL of the Millipore-purified water was added using an eppendorf reference pipette (Brinkmann Instruments, Inc., New York). This dilution was necessary because the luminescence spectrometer used to analyze the samples requires a minimum sample volume of 2 mL. The sample cuvettes were then sealed with plastic cuvette lids (Fisher Scientific, New Jersey). Ambient air temperature and thereby the temperature of water was maintained throughout the experiments at 21°C. The base case experiment was first conducted to determine background curves for Uranine (conservative tracer) and the two different-sized microsphere suspensions (colloids) in the absence of acoustic waves (0Hz). Subsequent flowthrough experiments were conducted using the same procedure described for the base case, but in the presence of acoustic waves at eight different preselected acoustic frequencies. Acoustic pressure at the influent was maintained at 3.33 psi (23.0 kPa). Due to different attenuation of acoustic waves at different frequencies, the acoustic pressure at the effluent was different depending upon frequency. Generally effluent pressure remained constant throughout the experiment and was always less than the pressure at the influent.

3.3 Tracer Properties

Tracers are chemicals or small particles commonly used in the study of the hydrodynamic processes of many systems including rivers and estuaries, tidal zones, lakes and marshes, and groundwater aquifers. They are also used extensively in the laboratory to quantify and test theoretical analytical and numerical solutions to transport equations. Tracers may be categorized into many classes but the two most common classifications are conservative tracers, those that do not experience adsorption to the porous matrix nor decay on the timescale of the experiment or study, and nonconservative tracers, which may experience adsorption and/or decay. Therefore, when a mass of conservative tracer is injected into a packed column, the entire mass

is recovered or conserved in the effluent stream. Nonconservative tracers always lose some mass either through decay or adsorption to the porous media. In the case of these experiments, the colloids are considered to experience adsorption but not decay. Each experiment was run with one conservative tracer (Uranine) and two non-conservative tracers (red and blue microspheres). Uranine is a dissolved molecular solute whereas the microspheres, due to their size, are colloids. The method of analyzing any tracer depends on the physical and chemical properties of the tracer. Ion chromatography can be used for analysis of most ionic salt tracers such as potassium bromide and other such alkali halide tracers. Spectrophotometric analysis is possible for molecular solute tracers that absorb light at certain wavelengths. Gravimetric analysis, the physical capturing and weighing of the particles on a filter media, or particle counting, the measuring of the scattering of a laser beam passing through a sample, can be used for analysis of small particles such as colloids. Fluorescence analysis is possible for tracers that exhibit fluorescence or chemiluminescence. Fluorescence refers to the property of a chemical to emit radiation (usually visible or UV light) when excited by radiation of a lower wavelength. The physicochemical properties of the chemical must be such that electrons in lower energy orbitals can be excited to higher energy orbitals by absorbing energy when bombarded with light of a particular wavelength. These higher energy orbitals are unstable and therefore the electrons decay to their original orbitals. As their orbit decays, energy is emitted in the form of light of a higher wavelength. Chemicals that exhibit fluorescence typically have an excitation spectra (a band of wavelengths of light that will excite electrons) and an emission spectra (a band of wavelengths of light emitted by decaying electrons) each containing a maxima, or in some cases several relative maxima, which depend on the physical structure of the molecule. The advantage of using a tracer that fluoresces over other types of tracers is that very dilute concentrations can be detected. Analysis is also generally faster because the excitation and consequent emission is virtually instantaneous. Both types of tracers (i.e., molecular solute and colloids) used in these experiments were specifically selected because they exhibit fluorescence. This is advantageous because all three tracers can be detected at very

low concentration and all three can be detected using the same type of fluorescence analysis equipment.

3.3.1 Uranine

There are several reasons to use a conservative tracer in packed column experiments. Conservative tracers are commonly used in order to characterize certain parameters of the porous media or packed column (e.g., dispersion and dispersivity). In addition, the breakthrough curves of the conservative tracer give a basis of comparison to characterize the colloid breakthrough curves. Finally, the effects of acoustic wave propagation on the transport of a conservative tracer has been studied and documented [*Vogler and Chrysikopoulos*, 2002]. Again, because fluorescent microspheres were used as model colloids, a conservative tracer that exhibits fluorescence was also desirable so that the same equipment could used for analysis. However, in order to analyze samples containing three different fluorescent tracers, it was important to select a conservative tracer whose excitation and emission spectra did not interfere with those of the microspheres. After careful examination of the excitation and emission spectra of the microspheres and several different tracers, Fluorescein Sodium Salt ($C_{20}H_{10}Na_2O_5$) commonly known as Uranine (Fisher Scientific, New Jersey) was selected. Uranine has been widely used as a tracer in groundwater and surface water studies. It has a molecular weight of 376.28 g/mol, an excitation maxima at 463 nm, and a broad emission spectra.

3.3.2 Fluorescent Microspheres

Two suspensions of fluorescent-dyed polystyrene microspheres of different mean particle diameter were used as model colloids in these experiments. Microsphere suspensions are commercially available and are used commonly for testing of filtration media and systems, flow tracing and fluid mechanics, sedimentation and centrifugation studies, particle counter research and development, fluorescence microscopy,

and medical imaging. Made of polystyrene, which itself does not fluoresce, they contain fluorescent dyes incorporated into their polymer matrix. They are packaged as suspensions of one-percent solids by mass in water. Two different-colored suspensions were used in this experiment: red and blue. The colors actually refer to the color of the wavelengths of light in the emission spectra which is dependent upon the type of fluorescent dyes incorporated into the polystyrene. Each color of microsphere suspension is available in a number of different mean diameter sizes. The red microspheres selected have a measured mean diameter of 0.028 μm, an excitation maxima at 542 nm and an emission maxima at 612 nm. The blue microspheres selected have a measured mean diameter of 0.10 μm, an excitation maxima at 388 nm and an emission maxima at 447 nm.

3.4 Method of Sample Analysis

When all the column effluent samples containing different concentrations of the three tracers were collected for an experiment as described in Section 3.2, they were analyzed by performing emission scans with an Aminco-Bowman series 2 luminescence spectrometer (Thermo Spectronic, New York). This section will discuss how the AB2 is used for fluorescence analysis, how emission wavelength ranges were chosen to resolve the concentration of each tracer in a sample, a confidence analysis of the measured concentrations, and the procedure used for calibrating concentrations for each experiment.

3.4.1 AB2 Luminescence Spectrometer

The Aminco-Bowman series 2 luminescence spectrometer (AB2) is capable of performing many different types of fluorescence and luminescence analyses including excitation scans, emission scans, synchronous scans, time traces, qualitative analyses, and polarization. Emission scans were used to determine tracer concentrations

in the column effluent samples from these experiments. In an emission scan, the sample is continuously excited at one specific wavelength (usually the excitation maxima which is dependent upon the structure of the molecules and can be predetermined with an excitation scan) while a range of higher wavelengths is scanned for light emitted or fluoresced from the sample. Figure 3.5 is a schematic of the AB2 performing an emission scan. To perform an emission scan with the AB2, the sample

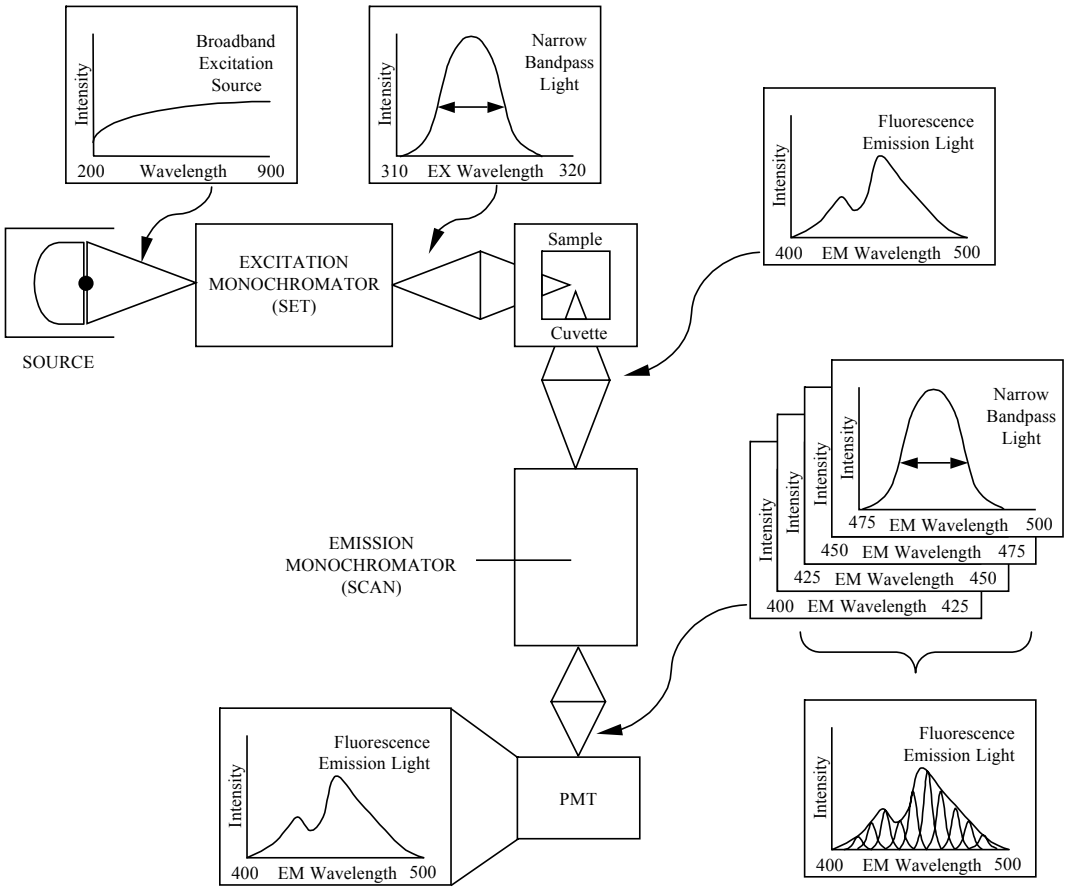

Figure 3.5: Schematic representation of the AB2 Luminescence Spectrometer performing an emission scan.

cuvette is placed in the sample compartment and the lid is closed to shut out all ambient light. The user then selects emission scan from the applications pull-down menu as the type of analysis to be performed. In a series of dialog boxes the user inputs a number of parameters for the scan such as the excitation wavelength, exci-

tation monochromator step size, bandpass, lower limit wavelength of the scan, upper limit wavelength of the scan, scan rate, and number of repetitions. The selection of these parameters will be discussed in Section 3.4.2. A 150 W ozone-free Xenon lamp provides a broadband excitation source in the range from 200-900 nm. The light passes through the excitation monochromator that was previously set by the user. A monochromator is a precision optical component consisting of diffraction gratings, mirrors, and slits used to select wavelength and bandpass values for excitation light and emitted light. The excitation monochromator selects a narrow bandwidth (group of wavelengths) from the source light. This narrow bandpass light is allowed to pass through while all other light from the source is diffracted. In the diagram, the light exiting the excitation monochromator is in the range of 310 to 320 nm. In reality, this is usually set at the excitation maxima of the sample. The excitation light is then passed through the cuvette containing the sample as a continuous beam where it excites the fluorescent molecules. The sample then emits a broad spectrum of light of higher wavelengths in all directions. This light is known as the sample's emission spectra, in this case in the range of 400 to 500 nm. Some of this emitted light passes through the emission monochromator which is positioned at 90 degrees to the excitation beam in order to avoid any interference. The emission monochromator selects a narrow bandwidth of emission wavelengths, in this case 400 to 425 nm. Again, the emission monochromator allows light of these wavelengths to pass through while deflecting all other wavelengths. This light from the emission monochromator illuminates the photocathode of the photomultiplier tube (PMT). The PMT then converts the light to an amplified DC current which is measured by the instruments acquisition electronics. The emission monochromator is then shifted by the step size (previously set) and another aquisition obtained. This process is repeated throughout the range of the emission scan. The AB2 automates this process so that you set excitation conditions and emission range and instrument collects the data and displays it as one continuous spectrum as in the final graph at the bottom right of Figure 3.5. Three separate emission scans were performed on each effluent sample corresponding to the three settings for each of the three tracers. Each

tracer's setting had an excitation maxima and emission wavelength range selected for that tracer. Thus it was possible to independently determine the concentration of Uranine, blue, and red microspheres in each sample. Before the samples could be analyzed it was necessary to carefully select excitation and emission wavelengths to minimize interference between the three tracers.

3.4.2 Excitation and Emission Wavelength Selection

Clearly an emission scan could be performed on any one constituent of the multicomponent tracer injection by itself, provided that the excitation wavelength maxima is known or can be determined. However, in order to determine the concentration of one tracer in a sample that contains the others, it was necessary to carefully select the emission wavelength ranges to allow for maximum fluorescence while minimizing any overlapping areas. Three emission scans with excitations at 412, 463, and 542 nm corresponding to the excitation maxima of blue microspheres, Uranine, and red microspheres respectively were performed on each of three samples. The three samples were single component samples: one of blue microspheres, one Uranine, and one red microspheres in the range of concentration they would be expected in the effluent. By plotting the three emission spectra (blue microspheres, Uranine, and red microspheres) at each excitation wavelength, it was possible to visually inspect for overlapping areas or cross-excitation. For instance, for the 412 nm excitation the blue microspheres showed a peak excitation in the range of 434 nm to 490 nm. However, the Uranine emission spectra for the 412 nm excitation wavelength began to increase from baseline at around 465 nm. The red microspheres did not emit with this excitation wavelength. Thus the emission spectrum range selected for the blue microspheres was from 434 nm to 464 nm. In this way, a sample containing blue microspheres, Uranine, and red microspheres could be excited at 412 nm and emission spectra recorded in the range 434 nm to 464 nm, and the result would be the same as a sample containing the same concentration of blue microspheres with no Uranine nor red microspheres present. The same procedure was repeated for

selection of all wavelength ranges. Table 3.2 summarizes the settings used for the emission scans. The ranges were then saved as global presets labeled in the computer as BLUE, URANINE, and RED. Thus each set of effluent samples and calibration dilutions for a given experiment was scanned under each of the three global presets and the concentration of each constituent tracer in the multicomponent tracer was determined.

3.4.3 Confidence of Measurements

Since the wavelength ranges were selected by visual inspection, it was necessary to test whether these settings were sufficient to properly resolve the concentrations of the three tracers in a single sample. To accomplish this, eleven dilutions were made with various amounts of the stock solutions to simulate effluent concentration curves where each tracer concentration was shifted by 2 minutes. We expect for the effluent concentration curves for the three tracers to either correspond to each other in each experiment (i.e., the peaks line up though the magnitudes are expected to be different) or to be shifted with respect to one another by a small amount. The most interference will occur if these shifts occur, so that if we can show the validity of measurements for shifted curves, this will also confirm the case of non-shifted curves. Figure 3.6 shows the concentration of each tracer in each of eleven dilutions containing different amounts of each tracer. Also included on the graph are error bars associated with each measurement. In general any one measurement of blue microspheres or Uranine was within two percent of actual while any one measurement of red was within four percent of actual. It was found that at higher concentrations there was more interference particularly with red microspheres. Therefore it was decided to use concentrations in the range of expected effluent concentrations for calibrating each experiment.

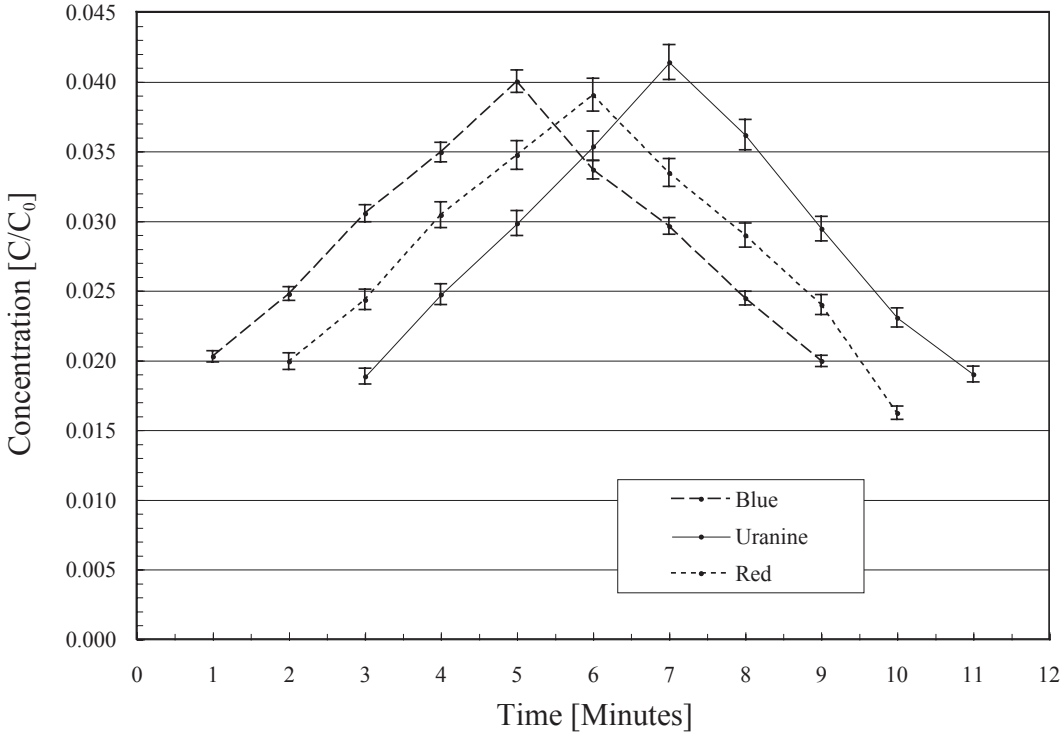

Figure 3.6: Multicomponent effluent sample concentrations made from dilutions of stock solutions to simulate a shifted curve.

3.4.4 Concentration Calibration

Section 3.2 stated that five dilutions of the initial multicomponent tracer injection were made at beginning of each experiment. At high concentrations there is more interference between the tracers so the desire was for the dilutions to be in the range of concentrations expected in the effluent. From prior packed column experiments it was known that the peak of the concentration curve would be approximately a one-in-twenty dilution of the actual injected concentration. Dilutions were made by pipetting 240, 300, 360, 420, and 480 μL of the multicomponent tracer injection into five 50 mL volumetric flasks and diluted to a final volume of 50 mL with purified water. The dilutions were then transferred into cuvettes, capped, and labeled C1 through C5 respectively. These were analyzed along with the samples and the

values plotted with concentration on the x-axis and fluorescence on the y-axis. A linear least-squares fit calibration curve was constructed and the value of the slope was used to convert effluent sample fluorescence measurements into concentration. In order to compare concentration breakthrough curves for Uranine and blue and red microspheres on the same graph it was necessary to make the curves of the same scale. The concentrations of Uranine and red and blue microspheres used in the multicomponent tracer injection were selected due to the intensity of the light they emitted, without regard to a physical concentration. As a result, the injected multicomponent tracer solution was 1.67 mg/L Uranine and 0.067 μg/L of both microspheres. The concentrations of microspheres reported as mass per volume are smaller by nearly five orders of magnitude than those of Uranine. This can be explained by considering that Uranine is molecular level solute and the microspheres are considerably larger particles. The microspheres have large surface areas covered with fluorescent dye and therefore emit more light and require a smaller mass concentration to measure. In addition, a mass concentration of microspheres includes both the polystyrene polymer and the fluorescent dyes incorporated into them. Therefore units of concentration such as mg/L and μg/L are not particularly meaningful when considering colloidal particles. A dimensionless concentration was used to compare concentrations of all the tracers. The concentrations are reported as C/C_0, where C is the measured tracer concentration in the effluent and C_0 is the concentration of the tracer injected. C/C_0, then, is the percentage of the initial injected tracer concentration in the effluent.

Table 3.2: Emission Scan Settings

Blue Microspheres		
Sensitivity	Auto Range C_0 at 85%	
Excitation	Wavelength	412 nm
	Step size	1.0 nm
	Bandpass	4 nm
Emission Scan	Lower	434 nm
	Upper	464 nm
	Scan rate	1.0 nm/sec
	Repititions	1
Uranine		
Sensitivity	Auto Range C_0 at 85%	
Excitation	Wavelength	463 nm
	Step size	1.0 nm
	Bandpass	4 nm
Emission Scan	Lower	500 nm
	Upper	600 nm
	Scan rate	3.0 nm/sec
	Repititions	1
Red Microspheres		
Sensitivity	Auto Range C_0 at 85%	
Excitation	Wavelength	542 nm
	Step size	1.0 nm
	Bandpass	4 nm
Emission Scan	Lower	600 nm
	Upper	740 nm
	Scan rate	3.0 nm/sec
	Repititions	1

Chapter 4

MATHEMATICAL MODEL DEVELOPMENT

The one-dimensional advection-dispersion equation for colloidal particles in homogeneous saturated porous media with adsorption (or filtration) and inactivation was derived from mass balance equations of a control volume under a constant hydraulic gradient and is given by the following linear second-order partial differential equation:

$$\frac{\partial C(t,x)}{\partial t} + \frac{\rho}{\theta}\frac{\partial C^*(t,x)}{\partial t} = D_e\frac{\partial^2 C(t,x)}{\partial x^2} - U_e\frac{\partial C(t,x)}{\partial x} - \lambda C(t,x) - \lambda^*\frac{\rho}{\theta}C^*(t,x), \quad (4.1)$$

where C is the concentration of colloids in suspension [M/L^3], C^* is the mass of colloids adsorbed on the solid matrix [M/M], D_e is the effective hydrodynamic dispersion coefficient [L^2/t], U_e is the effective interstitial fluid velocity [L/t], ρ is the bulk density of the porous media [M/L^3], λ is the inactivation constant of suspended colloids [t^{-1}], λ^* is the inactivation constant of adsorbed colloids [t^{-1}], θ is the porosity of soil medium [-], and t is time [t]. The effective interstitial fluid velocity is defined as

$$U_e = U + U^*, \quad (4.2)$$

where U is the steady-state background interstitial fluid velocity [L/t], and U^* is the additional velocity component attributed to acoustic pressure [L/t]. Similarly, the

effective dispersion coefficient is defined as

$$D_e = D + D^* = (U + U^*)\alpha_L + \mathcal{D}_e = U_e\alpha_L + \mathcal{D}_e, \tag{4.3}$$

where $D = U\alpha_L + \mathcal{D}_e$ is the hydrodynamic dispersion coefficient [L^2/t], α_L is the longitudinal dispersivity [L], $\mathcal{D}_e = \mathcal{D}/\tau^*$ is the effective molecular diffusion coefficient [L^2/t] (where $\mathcal{D}$ is the molecular diffusion coefficient [L^2/t], and $\tau^* > 1$ is the tortuosity coefficient [-]), and D^* is the additional dispersion component attributed to acoustic pressure [L^2/t]. It should be noted that the concept of effective parameters has been applied in numerous groundwater flow and solute transport studies [*Valocchi*, 1989; *Chrysikopoulos et al.*, 1990, 1992; *Kabala and Sposito*, 1991; *Chrysikopoulos*, 1995; *Vogler and Chrysikopoulos*, 2002]. The rate of colloid attachment onto the solid matrix is described by the following first-order equation:

$$\frac{\rho}{\theta}\frac{\partial C^*(t,x)}{\partial t} = r_1 C(t,x) - r_2 C^*(t,x), \tag{4.4}$$

where r_1 is the forward rate coefficient [t^{-1}], and r_2 is the reverse rate coefficient [M/L^3/t]. It should be noted that (4.4) is a generalized expression which can be easily adapted to two different colloid attachment processes: nonequilibrium reversible adsorption and modified colloid filtration, [*Sim and Crysikopoulos*, 1995].

The desired expression for C^* is obtained by solving (4.4) subject to an initial condition of zero sorbed (or filtered) colloid concentration ($C^*(0,x) = 0$) as

$$C^*(t,x) = \frac{r_1\theta}{\rho}\int_0^t C(\tau,x)\exp\Big[-\frac{r_2\theta}{\rho}(t-\tau)\Big]d\tau. \tag{4.5}$$

In view of (4.2)–(4.5) the governing equation (4.1) can be written as

$$\begin{aligned}\frac{\partial C(t,x)}{\partial t} &= D_e\frac{\partial^2 C(t,x)}{\partial x^2} - U_e\frac{\partial C(t,x)}{\partial x} - \mathcal{A}C(t,x)\\ &\quad - \mathcal{B}\int_0^t C(\tau,x)\exp[-\mathcal{H}(t-\tau)]d\tau,\end{aligned} \tag{4.6}$$

where the following substitutions have been employed:

$$\mathcal{A} = r_1 + \lambda, \tag{4.7}$$

$$\mathcal{B} = r_1(\lambda^* - \mathcal{H}), \tag{4.8}$$

$$\mathcal{H} = \theta r_2/\rho. \tag{4.9}$$

For a semi-infinite one-dimensional porous medium, the appropriate initial and boundary conditions are given by

$$C(0,x) = 0, \tag{4.10}$$

$$-D_e\frac{\partial C(t,0)}{\partial x} + U_e C(t,0) = M_0\delta(t), \tag{4.11}$$

$$\frac{\partial C(t,\infty)}{\partial x} = 0, \tag{4.12}$$

where $M_0 = M_{inj}/A\theta$ is the mass injected over the cross-sectional area of the column (where M_{inj} is the injected mass [M], A is the cross sectional area of the porous medium [L^2], and θ is porosity [-]), and δ is the Dirac delta function [1/t]. Initial condition (4.10) establishes a zero background colloid concentration. Boundary condition (4.11) describes the flux influent pulse concentration. The downstream boundary condition (4.12) preserves concentration continuity for a semi-infinite system. The solution to the governing equation (4.6) subject to conditions (4.10)–(4.12) is obtained analytically following the methods of Lapidus and Amundson, 1952, Chrysikopoulos et al., 1990, and Sim and Chrysikopoulos, 1995. Taking Laplace transforms of (4.6) and (4.10)–(4.12) with respect to time and space yields

$$\begin{aligned} s\dot{\widetilde{C}}(s,\gamma) - \dot{C}(0,\gamma) &= D_e\left[\gamma^2\dot{\widetilde{C}}(s,\gamma) - \gamma\widetilde{C}(s,0) - \frac{d\widetilde{C}(s,0)}{dx}\right] \\ &\quad - U_e[\gamma\dot{\widetilde{C}}(s,\gamma) - \widetilde{C}(s,0)] - \mathcal{A}\dot{\widetilde{C}}(s,\gamma) \\ &\quad - \frac{\mathcal{B}}{s+\mathcal{H}}\dot{\widetilde{C}}(s,\gamma), \end{aligned} \tag{4.13}$$

$$\dot{C}(0,\gamma) = 0, \tag{4.14}$$

$$-D_e\frac{d\widetilde{C}(s,0)}{dx} + U_e\widetilde{C}(s,0) = M_0, \tag{4.15}$$

$$\frac{d\widetilde{C}(s,\infty)}{dx} = 0, \tag{4.16}$$

where the following properties of Laplace transform were employed [*Roberts and Kaufman*, 1966]

$$\dot{\widetilde{C}}(s,\gamma) = \int_0^\infty\int_0^\infty C(t,x)e^{-st}e^{-\gamma x}dxdt, \tag{4.17}$$

$$\mathcal{L}\left\{C_{t^2}(t)\right\} = s^2\widetilde{C}(s) - sC(0) - C_t(0), \tag{4.18}$$

$$\mathcal{L}\left\{\int_0^t C(\tau)d\tau\right\} = \frac{C(s)}{s}, \tag{4.19}$$

$$\mathcal{L}\left\{e^{bt}\right\} = \frac{1}{s-b}. \tag{4.20}$$

The "tilde" and solid "dot" signify Laplace transform with respect to time and space, respectively, and s and γ are the corresponding Laplace domain variables. Substituting boundary conditions (4.14) and (4.15) into (4.13) and solving for $\dot{\widetilde{C}}(s,\gamma)$ yields

$$\dot{\widetilde{C}}(s,\gamma) = \frac{\gamma\widetilde{C}(s,0) - \dfrac{M_0}{D_e}}{\left(\gamma - \dfrac{U_e}{2D_e}\right)^2 - \left(\dfrac{s}{D_e} + \dfrac{\mathcal{A}}{D_e} + \dfrac{U_e^2}{4D_e^2} + \dfrac{\mathcal{B}}{D_e(s+\mathcal{H})}\right)}. \tag{4.21}$$

For mathematical convenience let

$$\begin{cases} M = -\dfrac{U_e}{2D_e} & (<0), \\ N = \left(\dfrac{s}{D_e} + \dfrac{\mathcal{A}}{D_e} + \dfrac{U_e^2}{4D_e^2} + \dfrac{\mathcal{B}}{D_e(s+\mathcal{H})}\right)^{1/2} & (>0). \end{cases} \tag{4.22}$$

Substituting (4.22) into (4.21) yields

$$\begin{aligned} \dot{\widetilde{C}}(s,\gamma) &= \frac{\gamma\widetilde{C}(s,0) - \dfrac{M_0}{D_e}}{(\gamma+M)^2 - N^2} \\ &= \frac{\gamma\widetilde{C}(s,0)}{(\gamma+M+N)(\gamma+M-N)} - \frac{\dfrac{M_0}{D_e}}{(\gamma+M+N)(\gamma+M-N)}. \end{aligned} \tag{4.23}$$

The above equation is easily inverted from the Laplace space variable γ back to the space variable x. The first term on the right hand side of (4.23) is inverted as follows

$$\mathcal{L}^{-1}\left\{\frac{\gamma}{(\gamma+M+N)(\gamma+M-N)}\right\} = \frac{(M+N)e^{-(M+N)x} - (M-N)e^{-(M-N)x}}{2N}, \tag{4.24}$$

similarly, the Laplace inversion of the second term at the right hand side of (4.23) is given by

$$\mathcal{L}^{-1}\left\{\frac{1}{(\gamma+M+N)(\gamma+M-N)}\right\} = \frac{e^{-(M-N)x} - e^{-(M+N)x}}{2N}, \tag{4.25}$$

where the following Laplace inversion identities were utilized [*Roberts and Kaufman*, 1966]

$$\mathcal{L}^{-1}\left\{\frac{\gamma}{(\gamma+\alpha_1)(\gamma+\alpha_2)}\right\} = \frac{\alpha_1 e^{-\alpha_1 x}}{\alpha_1-\alpha_2} + \frac{\alpha_2 e^{-\alpha_2 x}}{\alpha_2-\alpha_1}, \tag{4.26}$$

$$\mathcal{L}^{-1}\left\{\frac{1}{(\gamma+\alpha_1)(\gamma+\alpha_2)}\right\} = \frac{e^{-\alpha_1 x} - e^{-\alpha_2 x}}{\alpha_2-\alpha_1}. \tag{4.27}$$

Applying (4.24) and (4.25) into (4.23) yields

$$\begin{aligned}\widetilde{C}(s,x) &= \widetilde{C}(s,0)\Big[\frac{(M+N)e^{-(M+N)x} - (M-N)e^{-(M-N)x}}{2N}\Big] \\ &\quad - \frac{M_0}{D_e}\Big[\frac{e^{-(M-N)x} - e^{-(M+N)x}}{2N}\Big].\end{aligned} \tag{4.28}$$

Evaluation of $\widetilde{C}(s,0)$ can be easily done by taking the derivative with respect to x of (4.28) and, recalling boundary condition (4.16), setting the result equal to zero:

$$\begin{aligned}\frac{d\widetilde{C}(s,x)}{dx} &= \widetilde{C}(s,0)\Big[\frac{-(M+N)^2 e^{-(M+N)x} + (M-N)^2 e^{-(M-N)x}}{2N}\Big] \\ &\quad - \frac{M_0}{D_e}\Big[\frac{-(M-N)e^{-(M-N)x} + (M+N)e^{-(M+N)x}}{2N}\Big] \\ &= 0.\end{aligned} \tag{4.29}$$

Rearranging (4.29), taking the limit as $x \to \infty$, and recalling from (4.22) that $M < 0$ and $N > 0$ yields

$$\widetilde{C}(s,0) = -\frac{M_0}{D_e}\frac{1}{M-N}. \tag{4.30}$$

Substituting (4.30) into (4.28) and arranging the resulting equation yields

$$\widetilde{C}(s,x) = -\frac{M_0}{D_e}\frac{e^{-(M+N)x}}{(M-N)}. \tag{4.31}$$

Resubstituting M and N as they were defined in (4.22) into (4.31) yields

$$\widetilde{C}(s,x) = \frac{M_0}{\sqrt{D_e}}\exp\Big[\frac{U_e x}{2D_e}\Big]\frac{\exp\Big[-\frac{x}{\sqrt{D_e}}\Big(s+\mathcal{A}+\frac{U_e^2}{4D_e}+\frac{\mathcal{B}}{s+\mathcal{H}}\Big)^{1/2}\Big]}{\Big[\frac{U_e}{2\sqrt{D_e}}+\Big(s+\mathcal{A}+\frac{U_e^2}{4D_e}+\frac{\mathcal{B}}{s+\mathcal{H}}\Big)^{1/2}\Big]}. \tag{4.32}$$

For simplicity, (4.32) is rewritten as

$$\widetilde{C}(s,x) = \frac{M_0}{\sqrt{D_e}}\exp\Big[\frac{U_e x}{2D_e}\Big]\Theta, \tag{4.33}$$

where the following substitution is employed

$$\Theta = \frac{\exp\left[-\frac{x}{\sqrt{D_e}}\left(s+\mathcal{A}+\frac{U_e^2}{4D_e}+\frac{\mathcal{B}}{s+\mathcal{H}}\right)^{1/2}\right]}{\left[\frac{U_e}{2\sqrt{D_e}}+\left(s+\mathcal{A}+\frac{U_e^2}{4D_e}+\frac{\mathcal{B}}{s+\mathcal{H}}\right)^{1/2}\right]}. \tag{4.34}$$

For reasons that will become clear, equation (4.33) is rewritten equivalently as

$$\widetilde{C}(s,x) = \frac{M_0}{\sqrt{D_e}}\exp\left[\frac{U_e x}{2D_e}\right]\left\{\mathcal{H}\frac{1}{s+\mathcal{H}}\Theta + \frac{s}{s+\mathcal{H}}\Theta\right\}. \tag{4.35}$$

The inverse Laplace transform of (4.35) can be found by using a similar technique to that of Lapidus and Amundson, 1952, given by

$$\mathcal{L}^{-1}\left\{\frac{1}{s+\mathcal{H}}\widetilde{f}\left(s+\mathcal{H}+\frac{a}{s+\mathcal{H}}\right)\right\} = e^{-\mathcal{H}t}\int_0^t J_0\left[2\sqrt{a\zeta(t-\zeta)}\right]f(\zeta)d\zeta, \tag{4.36}$$

where the arbitrary function $f(t)$ is the inverse Laplace transform of $\widetilde{f}(s)$, and J_0 is the Bessel function of zero order. It should be noted that the same technique has been employed to find inverse Laplace transforms of several different problems [*Chrysikopoulos et al.*, 1990] and [*Sim and Chrysikopoulos*, 1995].

First, consider the inverse Laplace transform of the first term containing the Laplace variable s in the right hand side of (4.35)

$$\frac{1}{s+\mathcal{H}}\Theta. \tag{4.37}$$

Note that the $\mathcal{H}$ in said term is ignored for now since the inverse Laplace transform of $\mathcal{H}$ is simply $\mathcal{H}$. In order to apply (4.36), we assume that

$$\frac{1}{s+\mathcal{H}}\Theta = \frac{1}{s+\mathcal{H}}\widetilde{f}\left(s+\mathcal{H}+\frac{a}{s+\mathcal{H}}\right), \tag{4.38}$$

or in other words, Θ has the form of

$$\widetilde{f}\left(s+\mathcal{H}+\frac{a}{s+\mathcal{H}}\right).$$

In view of (4.36) and (4.38) then, the inverse Laplace transform of (4.37) is

$$\mathcal{L}^{-1}\left\{\frac{1}{s+\mathcal{H}}\Theta\right\} = e^{-\mathcal{H}t}\int_0^t J_0\left[2\sqrt{a\zeta(t-\zeta)}\right]f(\zeta)d\zeta. \tag{4.39}$$

We must determine $f(\zeta)$, which is the inverse Laplace transform of Θ, in order to complete the inverse Laplace transform of (4.37). In view of (4.34), the Laplace transform of the arbitrary function $f(t)$, which is given by $\widetilde{f}(s)$ is assumed to be of the form

$$\widetilde{f}(s) = \frac{e^{-l\sqrt{s+d}}}{h + \sqrt{s+d}}. \tag{4.40}$$

This step is not obvious but is done because we know the inverse Laplace transform of (4.40). Thus $f(t)$ can be determined from the inverse Laplace transform of $\widetilde{f}(s)$ using Laplace transform tables as [*Roberts and Kaufman*, 1966; *Spiegel*, 1990; *Sim and Chrysikopoulos*, 1995]

$$\begin{aligned} f(t) &= \mathcal{L}^{-1}\{\widetilde{f}(s)\} \\ &= \frac{\exp\left[\dfrac{-l^2}{4t} - dt\right]}{\sqrt{\pi t}} - h\exp\left[lh + \left(h^2 - d\right)t\right]\operatorname{erfc}\left[\frac{l}{2\sqrt{t}} + h\sqrt{t}\right]. \end{aligned} \tag{4.41}$$

The unknown constants h, l, d, and a are determined using the assumption given in (4.38) as follows. First, the left hand side of (4.38) is rearranged as

$$\begin{aligned} \frac{1}{s+\mathcal{H}}\Theta &= \frac{1}{s+\mathcal{H}} \frac{\exp\left[-\dfrac{x}{\sqrt{D_e}}\left(s + \mathcal{A} + \dfrac{U_e^2}{4D_e} + \dfrac{\mathcal{B}}{s+\mathcal{H}}\right)^{1/2}\right]}{\left[\dfrac{U_e}{2\sqrt{D_e}} + \left(s + \mathcal{A} + \dfrac{U_e^2}{4D_e} + \dfrac{\mathcal{B}}{s+\mathcal{H}}\right)^{1/2}\right]} \\ &= \frac{1}{s+\mathcal{H}} \frac{\exp\left[-\dfrac{x}{\sqrt{D_e}}\left(\dfrac{s^2 + \left(\mathcal{H} + \mathcal{A} + \dfrac{U_e^2}{4D_e}\right)s + \left(\mathcal{A} + \dfrac{U_e^2}{4D_e}\right)\mathcal{H} + \mathcal{B}}{s+\mathcal{H}}\right)^{1/2}\right]}{\left[\dfrac{U_e}{2\sqrt{D_e}} + \left(\dfrac{s^2 + \left(\mathcal{H} + \mathcal{A} + \dfrac{U_e^2}{4D_e}\right)s + \left(\mathcal{A} + \dfrac{U_e^2}{4D_e}\right)\mathcal{H} + \mathcal{B}}{s+\mathcal{H}}\right)^{1/2}\right]}. \end{aligned} \tag{4.42}$$

Second, the correct form of the Laplace transform of the arbitrary function, $\widetilde{f}(s)$, is determined by substituting the variable s in (4.40) with $s + \mathcal{H} + \dfrac{a}{s+\mathcal{H}}$ from (4.36) as

$$\widetilde{f}\left(s + \mathcal{H} + \frac{a}{s+\mathcal{H}}\right) = \frac{\exp\left[-l\left(\dfrac{s^2 + (2\mathcal{H}+d)s + \mathcal{H}^2 + \mathcal{H}d + a}{s+\mathcal{H}}\right)^{1/2}\right]}{h + \left(\dfrac{s^2 + (2\mathcal{H}+d)s + \mathcal{H}^2 + \mathcal{H}d + a}{s+\mathcal{H}}\right)^{1/2}}. \tag{4.43}$$

Finally, in view of (4.43) the right hand side of (4.38) can be written as

$$\frac{1}{s+\mathcal{H}}\widetilde{f}\left(s+\mathcal{H}+\frac{a}{s+\mathcal{H}}\right)=\frac{1}{s+\mathcal{H}}\frac{\exp\left[-l\left(\dfrac{s^2+(2\mathcal{H}+d)\,s+\mathcal{H}^2+\mathcal{H}d+a}{s+\mathcal{H}}\right)^{1/2}\right]}{h+\left(\dfrac{s^2+(2\mathcal{H}+d)\,s+\mathcal{H}^2+\mathcal{H}d+a}{s+\mathcal{H}}\right)^{1/2}}. \tag{4.44}$$

By simple comparison of (4.42) and (4.44), the unknown constants are obtained as

$$h=\frac{U_e}{2\sqrt{D_e}}, \tag{4.45}$$

$$l=\frac{x}{\sqrt{D_e}}, \tag{4.46}$$

$$d=\mathcal{A}+\frac{U_e^2}{4D_e}-\mathcal{H}, \tag{4.47}$$

$$a=\mathcal{B}. \tag{4.48}$$

After substituting (4.45)-(4.48) into (4.39) and (4.41), we define the resulting function as

$$\begin{aligned}\Phi(t) &= e^{-\mathcal{H}t}\int_0^t J_0\left[2\sqrt{\mathcal{B}\zeta\,(t-\zeta)}\right]\left\{\frac{\exp\left[\dfrac{-x^2}{4D_e\zeta}+\left(\mathcal{H}-\mathcal{A}-\dfrac{U_e^2}{4D_e}\right)\zeta\right]}{\sqrt{\pi\zeta}}\right.\\ &\left.-\frac{U_e}{2\sqrt{D_e}}\exp\left[\frac{U_e x}{2D_e}+(\mathcal{H}-\mathcal{A})\,\zeta\right]\operatorname{erfc}\left[\frac{x}{2\sqrt{D_e\zeta}}+\frac{U_e}{2}\sqrt{\frac{\zeta}{D_e}}\right]\right\}d\zeta, \end{aligned}\tag{4.49}$$

Therefore, we obtain the inverse Laplace transform of (4.37) as

$$\mathcal{L}^{-1}\left\{\frac{1}{s+\mathcal{H}}\Theta\right\}=\Phi(t). \tag{4.50}$$

Now we will consider the inverse Laplace transform of the second term containing the Laplace variable s in the right hand side of (4.35)

$$\frac{s}{s+\mathcal{H}}\Theta, \tag{4.51}$$

which can be found using the following property of Laplace transforms

$$\mathcal{L}\left\{\frac{d\Phi(t)}{dt}\right\}=s\widetilde{\Phi}(s)-\Phi(0), \tag{4.52}$$

where again the "tilde" signifies the Laplace transform with respect to time of Φ. From the limits of the integral in (4.49) it is clear that $\Phi(0) = 0$. Taking the Laplace transform of both sides of (4.50) yields

$$\frac{1}{s+\mathcal{H}}\Theta = \widetilde{\Phi}(s). \tag{4.53}$$

substitution of (4.53) into (4.52) gives

$$\mathcal{L}\left\{\frac{d\Phi(t)}{dt}\right\} = \frac{s}{s+\mathcal{H}}\Theta. \tag{4.54}$$

Taking the inverse Laplace transform of both sides of (4.54) gives us

$$\Phi'(t) = \mathcal{L}^{-1}\left\{\frac{s}{s+\mathcal{H}}\Theta\right\}, \tag{4.55}$$

where $\Phi'(t)$ is the derivative with respect to t of $\Phi(t)$. In view of (4.50) and (4.55) the inverse Laplace transform of (4.35) is

$$\widetilde{C}(t,x) = \frac{M_0}{\sqrt{D_e}}\exp\left[\frac{U_e x}{2D_e}\right]\left\{\mathcal{H}\Phi(t) + \Phi'(t)\right\}. \tag{4.56}$$

Now we must evaluate $\Phi'(t)$. For mathematical convenience we rewrite (4.49) as

$$\Phi(t) = e^{-\mathcal{H}t}\int_0^t \Omega(t,\zeta)d\zeta, \tag{4.57}$$

where

$$\Omega(t,\zeta) = J_0\left[2\sqrt{\mathcal{B}\zeta\,(t-\zeta)}\right] f\,(\zeta)\,, \tag{4.58}$$

and $f(\zeta)$ was previously determined (see (4.41) and its final form in (4.49)). Using the Product Rule and taking the derivative with respect to t of both sides of (4.57) yields

$$\Phi'(t) = e^{-\mathcal{H}t}\cdot\frac{d}{dt}\left[\int_0^t \Omega(t,\zeta)d\zeta\right] - \mathcal{H}e^{-\mathcal{H}t}\int_0^t \Omega(t,\zeta)d\zeta, \tag{4.59}$$

In view of (4.57) notice that the second term on the right hand side of (4.59) is just

$$-\mathcal{H}\Phi(t). \tag{4.60}$$

The derivative in the first term on the right hand side of (4.59) can be evaluated using Leibniz's Integral Rule, which is stated as

$$\frac{d}{dc}\int_a^b f(x,c)dx = \int_a^b \frac{\partial}{\partial c}f(x,c)dx + f(b,c)\frac{db}{dc} - f(a,c)\frac{da}{dc}, \tag{4.61}$$

where a and b are functions of c [*Abramowitz and Stegun*, 1972]. For the case of

(4.59) we find the following are true

$$c = t, \tag{4.62}$$

$$a(t) = 0, \tag{4.63}$$

$$b(t) = t, \tag{4.64}$$

$$x = \zeta, \tag{4.65}$$

$$f = \Omega. \tag{4.66}$$

Substitution of (4.62)-(4.66) into (4.61) yields

$$\frac{d}{dt}\int_0^t \Omega(t,\zeta)d\zeta = \int_0^t \frac{\partial}{\partial t}\Omega(t,\zeta)d\zeta + \Omega(t,t)\frac{dt}{dt} - \Omega(0,t)\frac{d0}{dt}. \tag{4.67}$$

Because

$$\frac{dt}{dt} = 1, \tag{4.68}$$

$$\frac{d0}{dt} = 0, \tag{4.69}$$

(4.67) becomes

$$\frac{d}{dt}\int_0^t \Omega(t,\zeta)d\zeta = \int_0^t \frac{\partial}{\partial t}\Omega(t,\zeta)d\zeta + \Omega(t,t). \tag{4.70}$$

In view of (4.58), the second term on the right hand side of (4.67) is

$$\begin{aligned} \Omega(t,t) &= J_0(0)\cdot f(t) \\ &= f(t). \end{aligned} \tag{4.71}$$

Now the partial derivative in the first term on the right side of (4.70) can be evaluated as follows. In view of (4.58)

$$\begin{aligned} \frac{\partial}{\partial t}\Omega(t,\zeta) &= \frac{\partial}{\partial t}\left\{J_0\left[2\sqrt{\mathcal{B}\zeta\,(t-\zeta)}\right]f\,(\zeta)\right\} \\ &= f(\zeta)\cdot\frac{\partial}{\partial t}\left\{J_0\left[2\sqrt{\mathcal{B}\zeta\,(t-\zeta)}\right]\right\}. \end{aligned} \tag{4.72}$$

Application of the chain rule to the right hand side of (4.72) yields

$$f(\zeta)\cdot\frac{\partial}{\partial t}\left\{J_0\left[2\sqrt{\mathcal{B}\zeta\,(t-\zeta)}\right]\right\} = f(\zeta)\cdot J_0'\left[2\sqrt{\mathcal{B}\zeta\,(t-\zeta)}\right]\frac{\mathcal{B}\zeta}{\sqrt{\mathcal{B}\zeta(t-\zeta)}}. \tag{4.73}$$

From recurrence relations we have that

$$J_0'(u) = -J_1(u), \tag{4.74}$$

where $J_1(u)$ is the first order Bessel function. Substituion of (4.74) into (4.73) gives us

$$-f(\zeta) \cdot J_1\left[2\sqrt{\mathcal{B}\zeta(t-\zeta)}\right] \frac{\mathcal{B}\zeta}{\sqrt{\mathcal{B}\zeta(t-\zeta)}}, \tag{4.75}$$

and rearranging (4.75) we have obtained

$$\frac{\partial}{\partial t}\Omega(t,\zeta) = -f(\zeta) \cdot J_1\left[2\sqrt{\mathcal{B}\zeta(t-\zeta)}\right] \frac{\mathcal{B}\zeta}{\sqrt{\mathcal{B}\zeta(t-\zeta)}}. \tag{4.76}$$

Substituting (4.76) and (4.71) into (4.70) gives us

$$\frac{d}{dt}\int_0^t \Omega(t,\zeta)d\zeta = -\int_0^t \frac{\mathcal{B}\zeta}{\sqrt{\mathcal{B}\zeta(t-\zeta)}} \cdot J_1\left[2\sqrt{\mathcal{B}\zeta(t-\zeta)}\right] f(\zeta)d\zeta + f(t). \tag{4.77}$$

Substitution of (4.77) and (4.60) into (4.59) gives us

$$\Phi'(t) = -e^{-\mathcal{H}t}\int_0^t \frac{\mathcal{B}\zeta}{\sqrt{\mathcal{B}\zeta(t-\zeta)}} J_1\left[2\sqrt{\mathcal{B}\zeta(t-\zeta)}\right] f(\zeta)d\zeta + e^{-\mathcal{H}t}f(t) - \mathcal{H}\Phi(t). \tag{4.78}$$

Substituting (4.78) into (4.56) yields

$$\begin{aligned}\widetilde{C}(t,x) &= \frac{M_0}{\sqrt{D_e}}\exp\left[\frac{U_e x}{2D_e}\right]\left\{\mathcal{H}\Phi(t) - e^{-\mathcal{H}t}\int_0^t \frac{\mathcal{B}\zeta}{\sqrt{\mathcal{B}\zeta(t-\zeta)}} J_1\left[2\sqrt{\mathcal{B}\zeta(t-\zeta)}\right] f(\zeta)d\zeta\right. \\ &\quad \left. + e^{-\mathcal{H}t}f(t) - \mathcal{H}\Phi(t)\right\}.\end{aligned} \tag{4.79}$$

Note that the $\mathcal{H}\Phi(t)$ terms cancel. Rearranging (4.79) gives

$$\widetilde{C}(t,x) = \frac{M_0}{\sqrt{D_e}}\exp\left[\frac{U_e x}{2D_e} - \mathcal{H}t\right]\left\{f(t) - \int_0^t \frac{\mathcal{B}\zeta}{\sqrt{\mathcal{B}\zeta(t-\zeta)}} J_1\left[2\sqrt{\mathcal{B}\zeta(t-\zeta)}\right] f(\zeta)d\zeta\right\}. \tag{4.80}$$

Finally, substitution of $f(t)$ as it was defined in (4.49) into (4.80) results in the final solution:

$$
\begin{aligned}
C(t,x) = \frac{M_0}{\sqrt{D_e}} \exp\left[\frac{U_e x}{2D_e} - \mathcal{H}t\right] \Bigg\{ & \frac{\exp\left[\frac{-x^2}{4D_e t} + \left(\mathcal{H} - \mathcal{A} - \frac{U_e^2}{4D_e}\right)t\right]}{\sqrt{\pi t}} \\
& - \frac{U_e}{2\sqrt{D_e}} \exp\left[\frac{U_e x}{2D_e} + (\mathcal{H} - \mathcal{A})t\right] \operatorname{erfc}\left[\frac{x}{2\sqrt{D_e t}} + \frac{U_e}{2}\sqrt{\frac{t}{D_e}}\right] \\
& - \int_0^t \frac{\mathcal{B}\zeta}{\sqrt{\mathcal{B}\zeta(t-\zeta)}} J_1\left[2\sqrt{\mathcal{B}\zeta(t-\zeta)}\right] \left[\frac{\exp\left[\frac{-x^2}{4D_e\zeta} + \left(\mathcal{H} - \mathcal{A} - \frac{U_e^2}{4D_e}\right)\zeta\right]}{\sqrt{\pi\zeta}}\right. \\
& \left. - \frac{U_e}{2\sqrt{D_e}} \exp\left[\frac{U_e x}{2D_e} + (\mathcal{H} - \mathcal{A})\zeta\right] \operatorname{erfc}\left[\frac{x}{2\sqrt{D_e\zeta}} + \frac{U_e}{2}\sqrt{\frac{\zeta}{D_e}}\right]\right] d\zeta \Bigg\}. \qquad (4.81)
\end{aligned}
$$

Chapter 5

RESULTS AND DISCUSSION

5.1 Determination of Column Parameters

Before the analytical solution (equation 4.81) could be fit to the experimental breakthrough data, the parameters associated with the column and glass beads needed to be obtained. The relevant parameters were porosity of the column, θ, bulk density of the glass beads, ρ, and the average interstitial velocity, U. It should be noted that the variables $\mathcal{H}$ and U_e in equation 4.81 are combined parameters that contain θ, ρ, and U. Porosity of the solid matrix (bead-pack) is given by

$$\theta = \frac{V_{voids}}{V_{total}} = \frac{V_{total} - V_{beads}}{V_{total}}, \tag{5.1}$$

where V_{voids} is the volume of the void space inside the packed column [L^3]; V_{total} is the total inner volume of the glass column [L^3]; and V_{beads} is the volume of the glass beads themselves in the column [L^3]. The total volume was calculated from the inner diameter and length of the column. The volume of the beads in the column was determined by transferring the beads to a graduated cylinder filled with water and measuring the volume of water they displaced (Archimedes' Principle). The bulk density is given by

$$\rho = \frac{M_{beads}}{V_{total}}, \tag{5.2}$$

where M_{beads} is the mass of the beads [M]; and V_{total} is the total inner volume of the glass column [L^3] as before. The average interstitial velocity is given by

$$U = \frac{q}{\theta} = \frac{Q}{A\theta}, \tag{5.3}$$

where q is the seepage or Darcy velocity [L/t]; Q is the volumetric flow rate [L^3/t]; and A is the cross-sectional area of the columns [L^2]. The volumetric flow rate was set at 0.80 mL/min (see section 3.1) for all experiments and the cross-sectional area was calculated from the inner diameter of the column. The parameters are listed in Table 5.1.

Table 5.1: Column Parameters

Parameter	Symbol	Value
Porosity	θ	0.368 [-]
Bulk Density	ρ	1.60 [g/cm^3]
Average Interstitial Velocity	U	26.57 [cm/hr]

5.2 Effects of Various Model Parameters

Before analysis of the experimental data, a discussion of the effects of the various model parameters on the character of the breakthrough curves generated by the analytical solution is instructive. Figures 5.1, 5.2, 5.3, and 5.4 illustrate the effects of changing a single model parameter (namely U, D, k_c, and k_r), while keeping the other model parameters constant. These figures will facilitate some qualitative insight into the causes of the observed effects in the experimental data.

Figure 5.1 illustrates the effect of changing average interstitial velocities, U, while holding the other model parameters constant. The solution was plotted with U equal to 25, 26, 27, 28, and 29 cm/h. Examination of the graph shows that greater (faster)

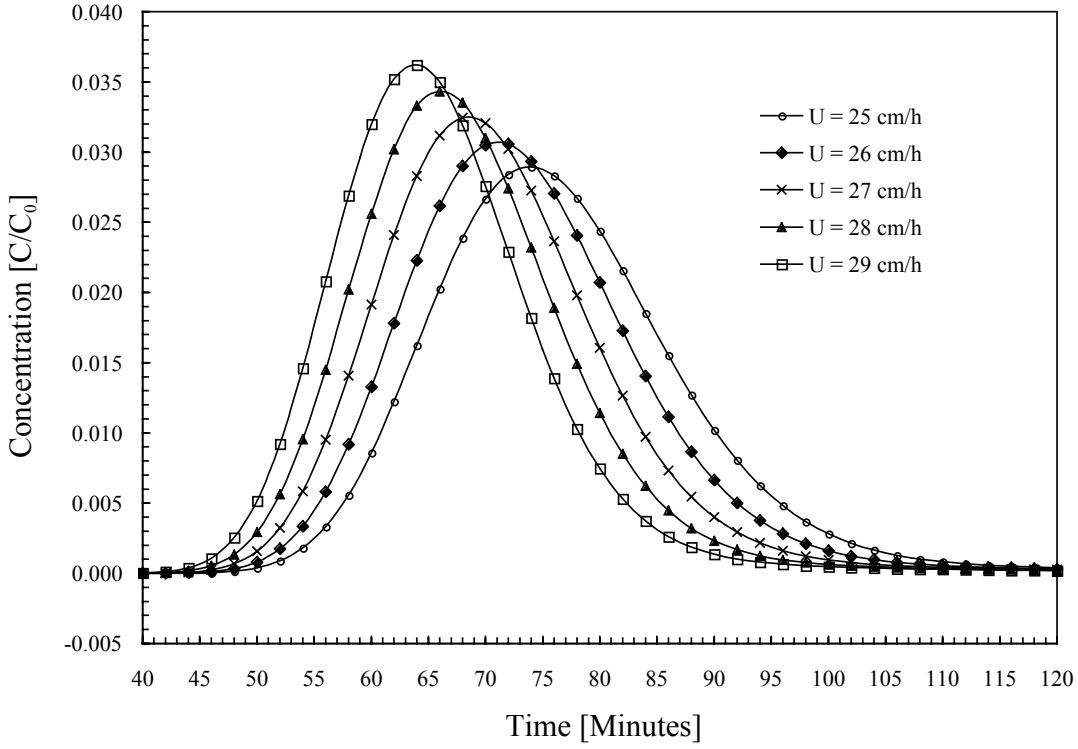

Figure 5.1: An illustration of the effect of average interstitial velocity, U, on the character of the analytical solution with $D = 7.0$ cm^2/h, $k_c = 5.0\text{E}{-}02$ 1/h, and $k_r = 2.5$ 1/h.

interstitial velocity causes the curve to shift to the left indicating a faster peak breakthrough (bulk mass shift). There is also less spreading of the faster breakthrough curve, though all the curves were generated with the same hydrodynamic dispersion coefficient. This is due solely to the faster-moving curve having less time to spread than the slower moving curve on the right. It should be noted that, in reality, increasing interstitial velocity also increases the hydrodynamic dispersion coefficient due to mechanical mixing (see equation 4.3).

Figure 5.2 shows the effect of changing the hydrodynamic dispersion coefficient on the solutuion. The solution was plotted with D equal to 5, 7, and 9 cm^2/h. Increasing hydrodynamic dispersion causes the curves to spread more in both directions (i.e.,

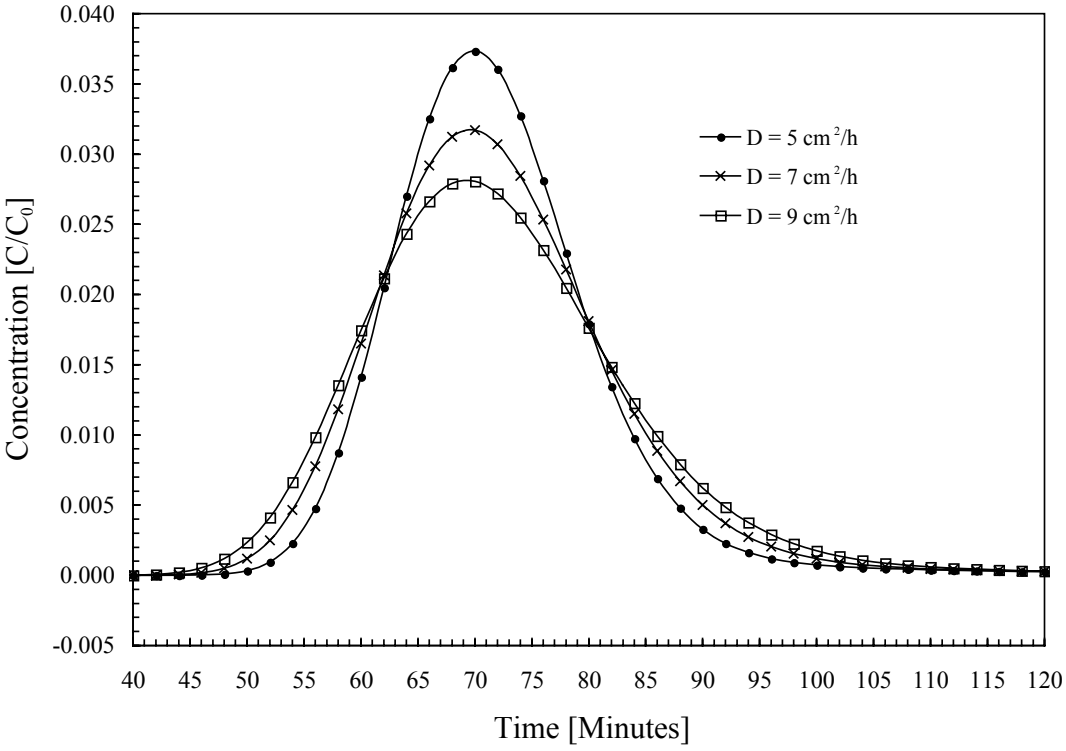

Figure 5.2: An illustration of the effect of hydrodynamic dispersion, D, on the analytical solution with $U = 26.57$ cm/h, $k_c = 5.0\text{E}{-}02$ 1/h, and $k_r = 2.5$ 1/h.

longitudinally). The concentration in the effluent begins to increase earlier if the hydrodynamic dispersion is greater, even when the interstitial velocity is the same. This does not constitute a bulk shift, however, because the peak breakthrough time does not change.

Figure 5.3 shows the effect of changing the forward rate coefficient on the solution. The solution was plotted with k_c equal to 5.0E-02, 1.1E-01, and 1.7E-01 1/h. In general r_1, or k_c, can be thought of as the rate of sorption or clogging. A larger r_1 causes a lower peak concentration and tailing of the curve with time. This is due to the tracer adsorbing to the solid matrix and detaching later. Thus k_c can cause a bulk shift only to the right and tailing only at later times. We must recall that, as evinced in equation 4.4, k_c and k_r work in conjuction to affect the character of the

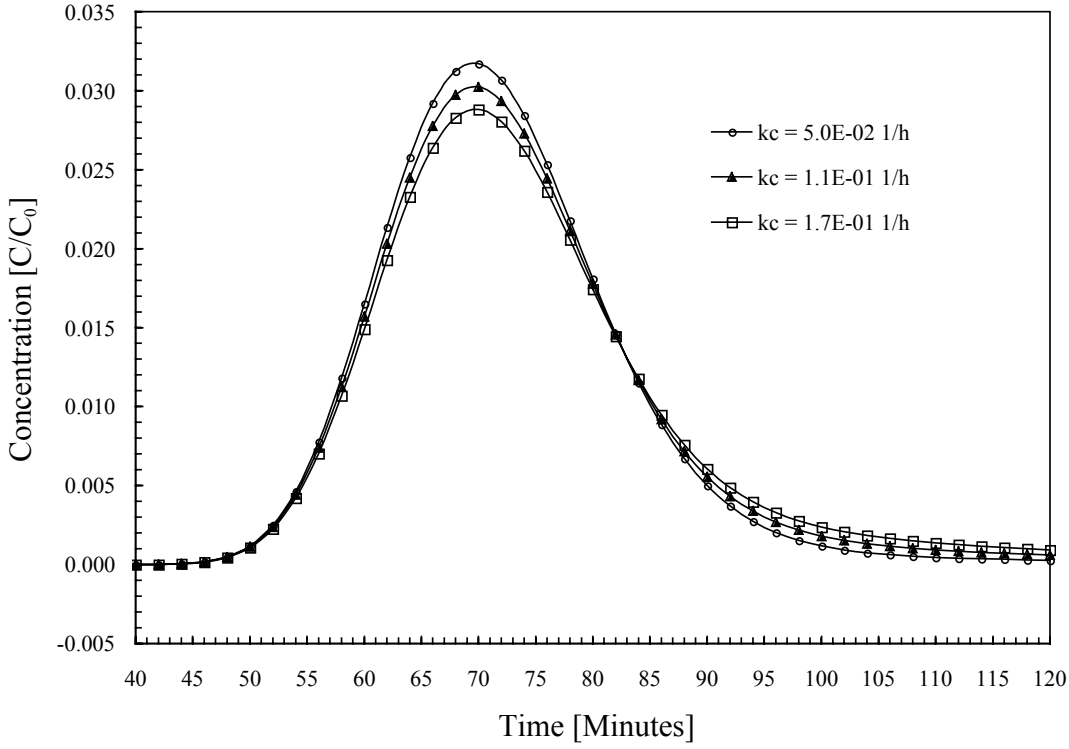

Figure 5.3: An illustration of the effect of the forward rate constant, k_c, on the character of the analytical solution with $U = 26.57$ cm/h, $D = 7.0$ cm^2/h, and $k_r = 2.5$ 1/h.

solution.

Figure 5.4 illustrates the effect of changing the reverse rate coefficient on the solution. The solution was plotted with k_r equal to 2.5, 0.10, and 0.01 1/h. In general r_2, or k_r, is the rate of release of adsorbed tracer. In this case the effect of k_r is difficult to discern because the value of k_c is very small.

5.3 Experimental Results

Subsequently, the Levenberg-Marquardt nonlinear least squares regression method was used with the analytical solution to determine the effective dispersion coefficient

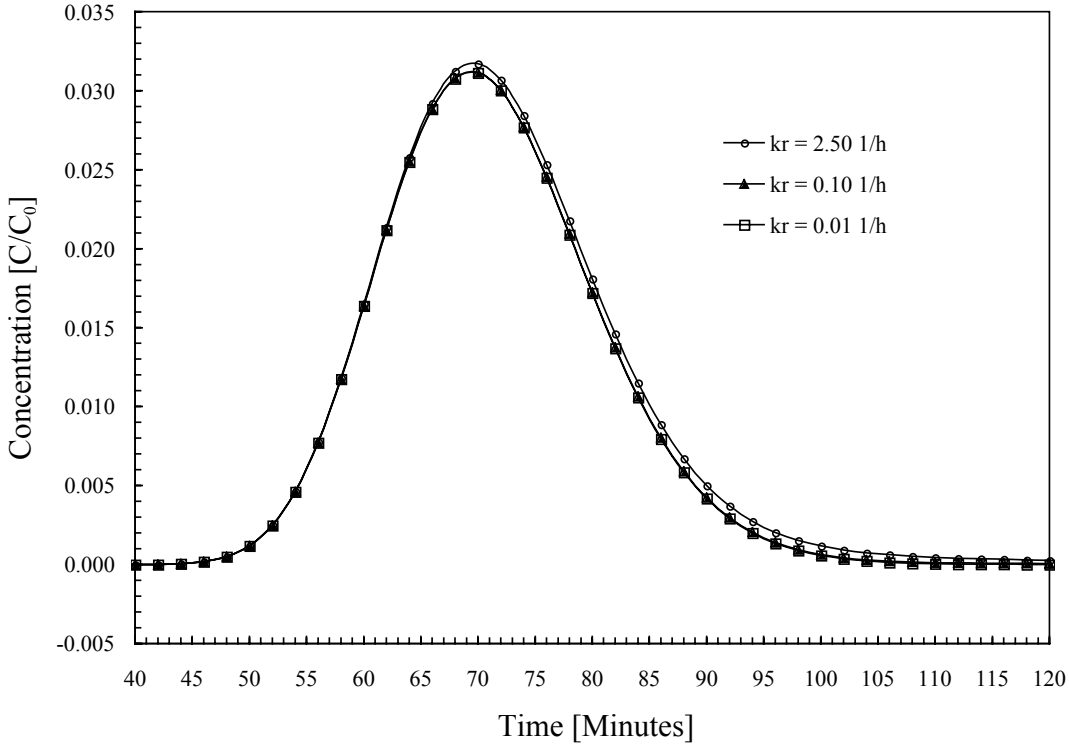

Figure 5.4: An illustration of the effect of the reverse rate constant, k_r, on the analytical solution with $U = 26.57$ cm/h, $D = 7.0$ cm^2/h, and $k_c = 5.0\text{E}{-}02$ 1/h.

and the effective velocity associated with each acoustic frequency. By comparing the values of effective dispersion and effective velocity at a particular frequency with the values of the base case (no acoustics), it is possible to determine D^* and U^*, the components of these parameters attributable to acoustic pressure. For the equation relating these parameters, see equations 4.2 and 4.3. The objective of the nonlinear least squares method is to obtain estimates of the model parameters that minimize the sum of squared residuals between simulated and observed data. The program utilizes the subroutine mrqmin for fitting the data and the subroutine qdag for numerical evaluation of the integral present in equation 4.81.

Figure 5.5 shows the base case experimental data for Uranine and the two colloids along with the fitted analytical solution for that data. These curves are characteristic

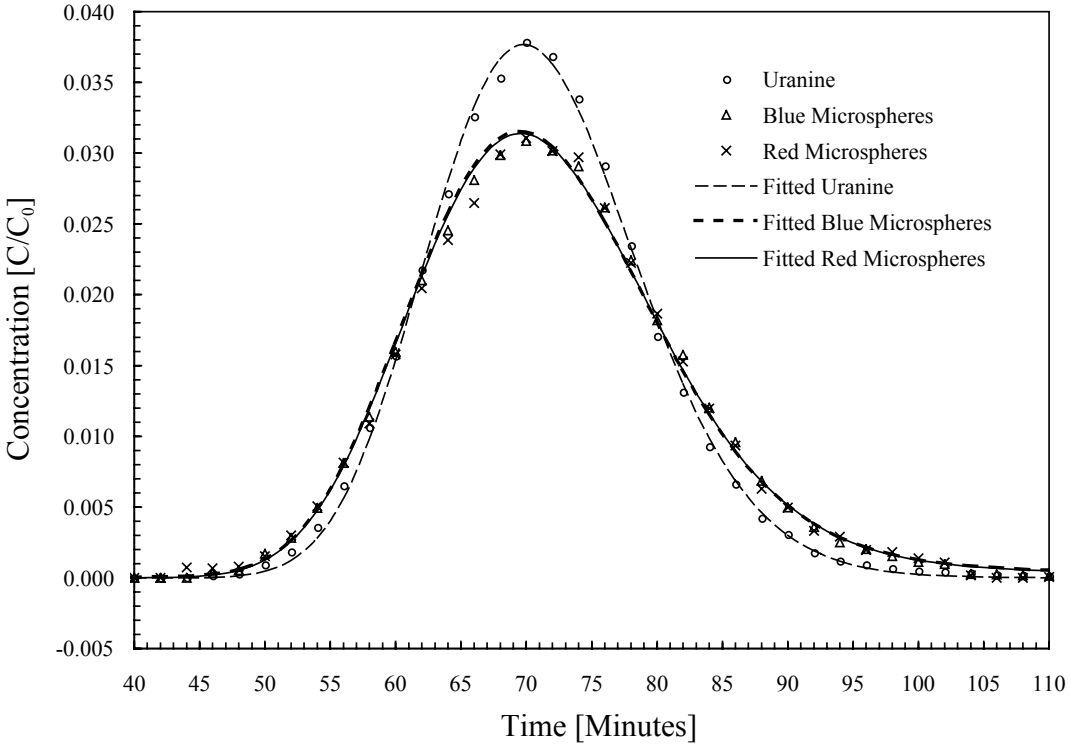

Figure 5.5: The symbols are the experimental data for the Base Case (No Acoustic Pressure) for Uranine, blue, and red microspheres. The solid lines are the fitted analytical solutions.

of the curves at all frequencies tested in that the peak concentration of Uranine is always higher than that of blue or red microspheres, while the microspheres exhibit more tailing at later times. For this experimental set-up, there is very little discernable difference between the blue and red microspheres (colloids with difference diameters). It should also be noted that there is no observed early breakthrough for colloids over the conservative tracer as might be expected (see section 2.3.2). The early breakthrough effect is due to size exclusion which should not be present in this column because the pore space in 2 mm glass beads is quite large. The calculated value of interstitial velocity, U, was used and dispersion, D, was fit from experimental data. The fitted base case hydrodynamic dispersion for Uranine, blue, and red microspheres was 5.35, 7.07, and 7.12 cm^2/h, respectively. In addition r_1 and r_2 were

fit for the blue and red microspheres. The fitted values of r_1 and r_2 for blue and red microspheres were 5.38E-02 h^{-1} and 2.49 h^{-1}; and 5.31E-02 h^{-1} and 2.51 h^{-1}, respectively. They were considered to be constant at different acoustic frequencies. For experiments conducted with acoustic pressure oscillation, the values obtained from fitting were actually U_e and D_e (See equations 4.2 and 4.3). The values obtained from the base case were subtracted from these to obtain the components attributed to acoustics, which are depicted graphically in Figures 5.8 and 5.9. For the low velocity used in these experiments, the small deposition rates obtained agree with the literature as the experimental work of Kretzschmar and Sticher, 1998, suggested a direct relationship between deposition rates and pore velocity.

Figure 5.6 shows experimental and fitted solution for Uranine for the base case, 90 Hz, and 30 Hz acoustic oscillation frequency. The acoustic influent pressure was maintained at 3.33 psi (23.0 kPa). It should be noted that there is different attenuation of pressure waves at different frequecies, which causes there to be a different acoustic pressure gradient along the column even when the influent pressure is the same.

The acoustic pressure gradient along the column is given by

$$\Delta P = \frac{P_2 - P_1}{L}, \tag{5.4}$$

where ΔP is the acoustic pressure gradient [kPa/cm]; P_2 is the acoustic pressure at the effluent end of the column [kPa]; P_1 is the acoustic pressure at the influent end of the column [kPa]; and L is the length of the column [cm]. Figure 5.7 shows the acoustic pressure gradient along the column at different frequencies. For the frequencies studied in these experiments the attenuation appears to be roughly linearly and inversely related to frequency. At higher frequencies there is less attenuation in the column.

Similar effects were observed for colloids as well with the exception of lower peak concentrations and tailing, just as in the base case. The analytical solution fit the experimental data well.

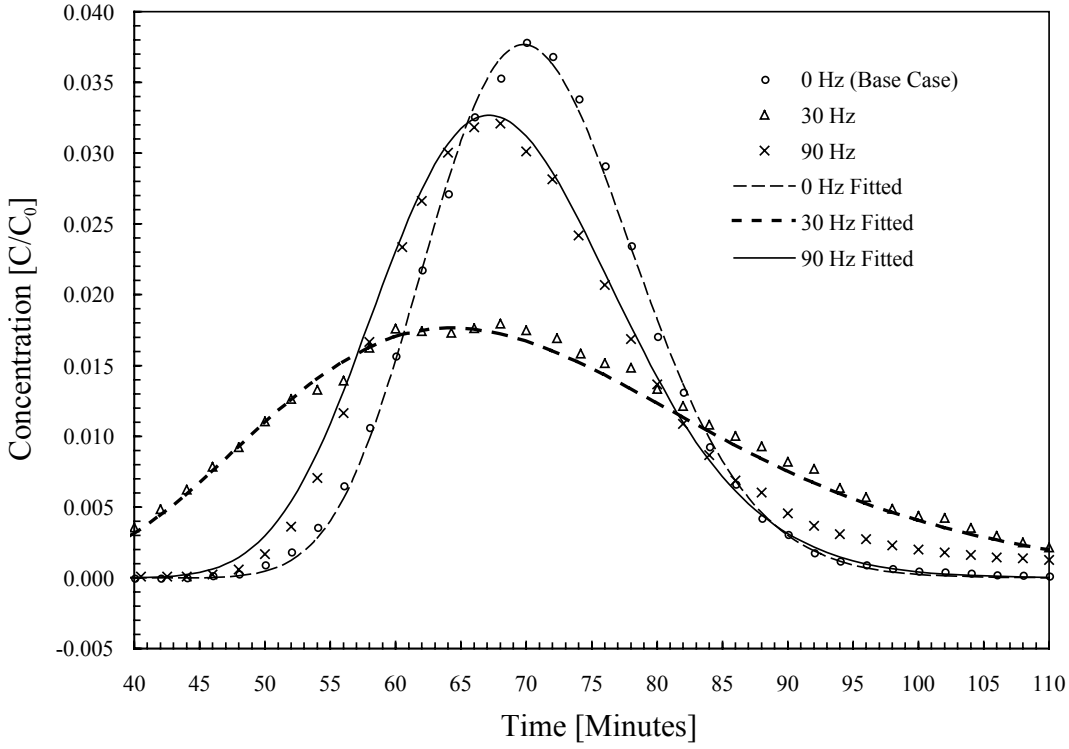

Figure 5.6: The symbols are the experimental data for Uranine for the Base Case, 90 Hz, and 30 Hz. The lines are the fitted analytical solutions.

The results of the experiments are displayed in Figures 5.8, 5.9, and 5.10 showing the components of interstitial velocity and hydrodynamic dispersion attributed to acoustics at each acoustic frequency tested.

Acoustic pressure forcing caused an increase in interstitial velocity at all frequencies for the conservative tracer and colloids of both size. The maximum increase in velocity occurred at 70 Hz. Acoustics also caused increased dispersion above the base case at all frequecies. There was a very large observed spike in dispersion at 30 Hz.

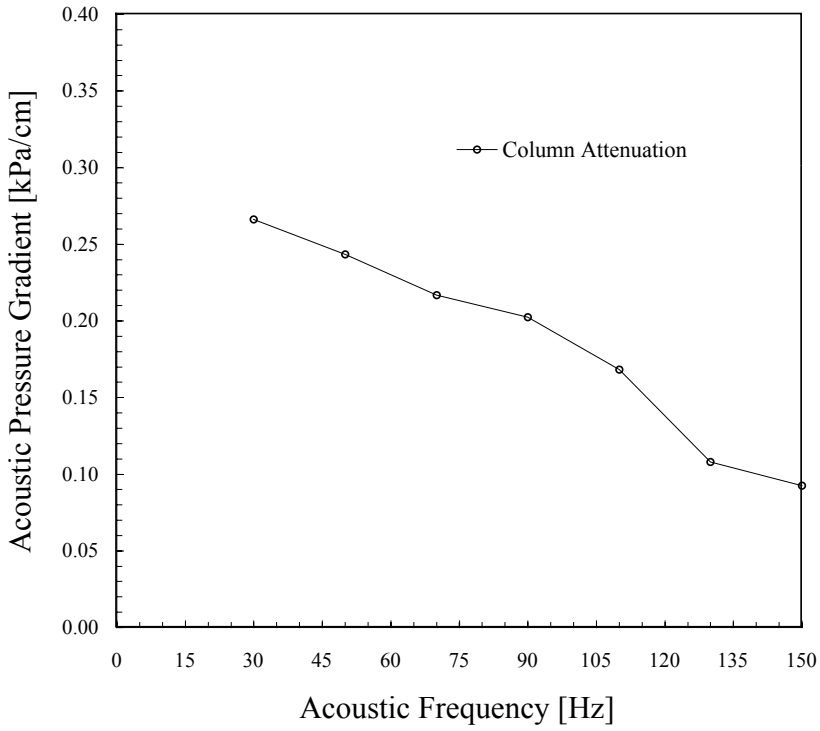

Figure 5.7: The acoustic pressure gradient along the column at different frequencies. A larger acoustic pressure gradient means greater attenuation.

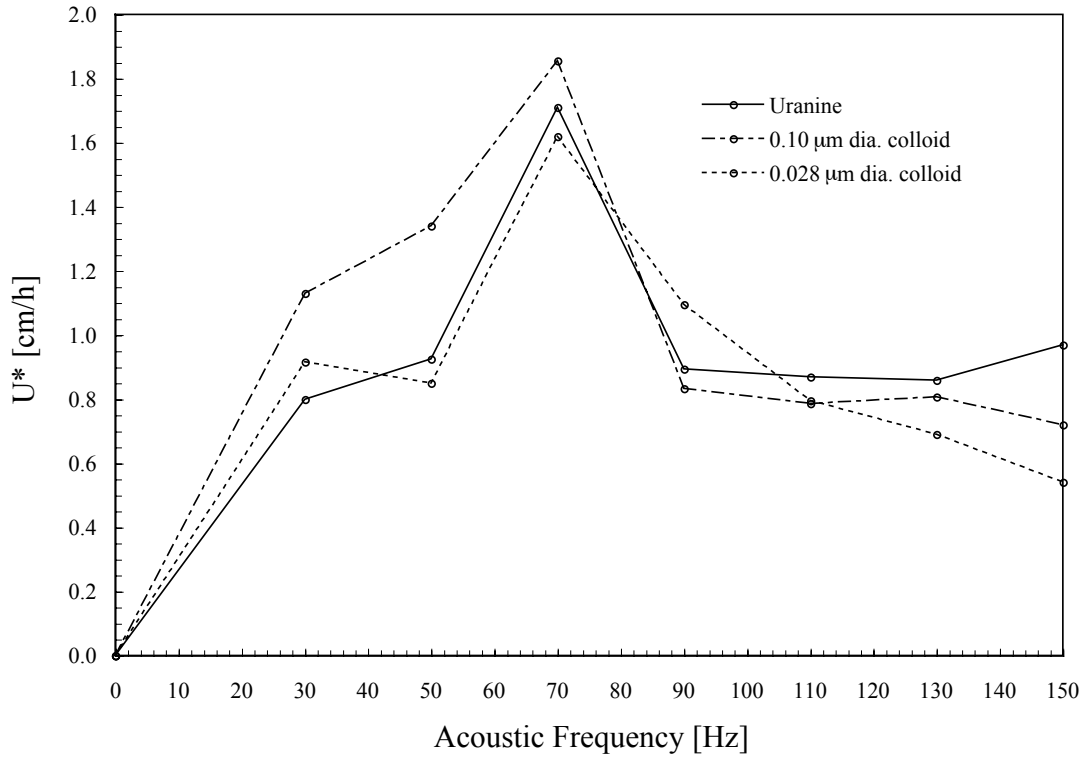

Figure 5.8: The component of effective interstitial velocity attributed to acoustics, U^*, (see Equation 4.2) versus the frequency of acoustic pressure oscillation for Uranine, blue, and red microspheres.

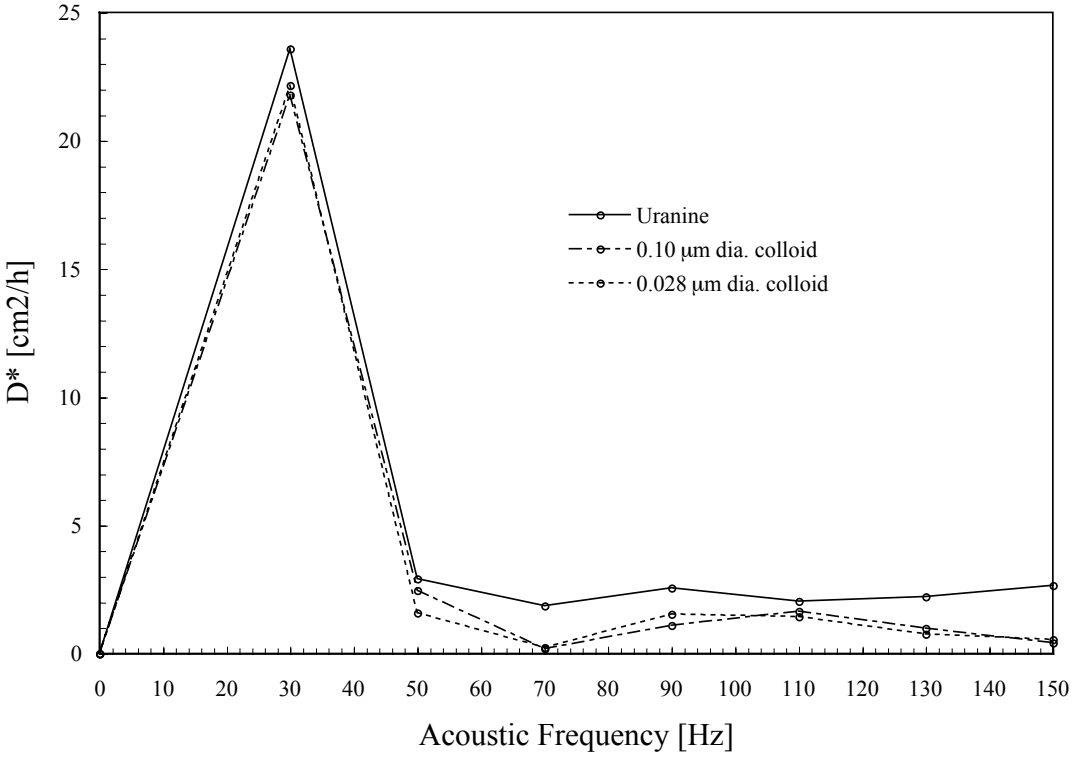

Figure 5.9: The component of effective hydrodynamic dispersion coefficient attributed to acoustics, D^*, (see Equation 4.3) versus frequency.

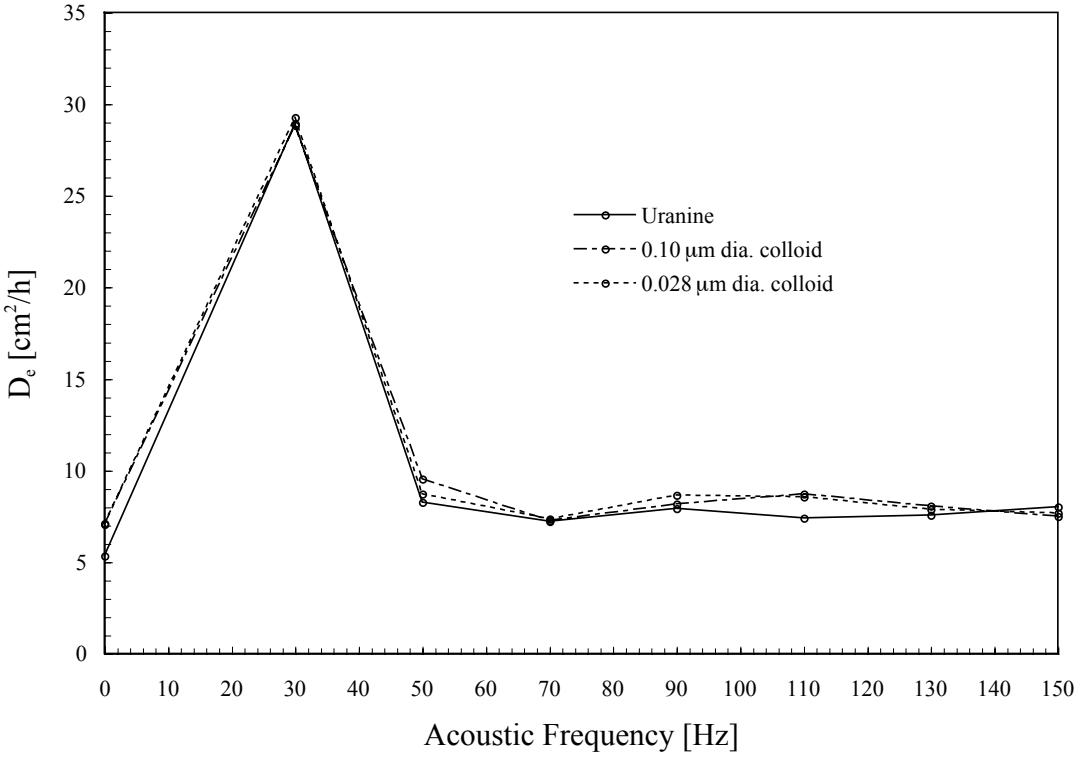

Figure 5.10: The effective hydrodynamic dispersion coefficient, D_e, (see Equation 4.3) versus frequency.

Chapter 6

CONCLUSIONS

Before analysis of the experimental data, a discussion of the effects of the various model parameters on the character of the breakthrough curves generated by the analytical solution was given. Figures 5.1, 5.2, 5.3, and 5.4 illustrate the effects of changing a single model parameter (namely U, D, k_c, and k_r), while keeping the other model parameters constant. Examination of the graph shows that greater (faster) effective interstitial velocity causes the curve to shift to the left indicating a faster peak breakthrough (bulk mass shift). There is also less spreading of the faster breakthrough curve due to decreased retention time. Increasing hydrodynamic dispersion causes the curves to spread more in both directions (i.e., longitudinally). The concentration in the effluent begins to increase earlier if the hydrodynamic dispersion is greater. A larger r_1 causes a lower peak concentration and tailing of the curve with time. In this case the effect of k_r is difficult to discern. These curves are characteristic of the curves at all frequencies tested in that the peak concentration of Uranine is always higher than that of blue or red microspheres, while the microspheres exhibit more tailing at later times. For this experimental set-up, there is very little discernable difference between the blue and red microspheres (colloids with difference diameters). It should also be noted that there is no observed early breakthrough for colloids over the conservative tracer as might be expected (see section 2.3.2). The fitted base case hydrodynamic dispersion for Uranine, blue, and red microspheres

was 5.35, 7.07, and 7.12 cm^2/h, respectively. The fitted values of r_1 and r_2 for blue and red microspheres were 5.38×10^{-2} h^{-1} and 2.49 h^{-1}; and 5.31×10^{-2} h^{-1} and 2.51 h^{-1}, respectively. Acoustic pressure forcing caused an increase in effective interstitial velocity at all frequencies for the conservative tracer and colloids of both size. The maximum increase in velocity occurred at 70 Hz. Acoustics also caused increased dispersion above the Base Case at all frequecies. There was a very large observed spike in dispersion at 30 Hz. Clearly applied acoustic pressure increases colloid transport. The exact mechanisms for this are still under investigation.

Chapter 7

PROPOSED RESEARCH

7.1 New Experimental Design

One of the main drawbacks to the current mechanism of introducing acoustic waves to the porous media is that it is impossible to quantify the volume of the fluid that is moving back and forth with each oscillation. This becomes important in many of the mathematical considerations of NAPL mobilization and dissolution, as well as in the ability to fully describe the dynamics involved in the enhanced transport processes described in this paper. The frequency and amplitude of the pressure oscillation are set with the function generator and amplifier but without knowing the actual throw of the transducer, the fluid volume cannot be determined. This will be overcome by design of a small piston attached to a rotating cam that will produce oscillatory forcing that can be measured absolutely, rather than a speaker. Figure 7.1 is a schematic of this new design. It is a less convenient method because the amplitude cannot be easily adjusted, but ultimately much better for characterizing oscillatory flow. This may make it possible to then directly relate the advection-dispersion equation to oscillatory flow, ultimately developing a solution as in equation 4.81 but that includes terms for frequency and amplitude of an applied acoustic field. This new design will also be versatile and easily adaptable to packed columns, monolayers,

and in the future perhaps even etched micromodels.

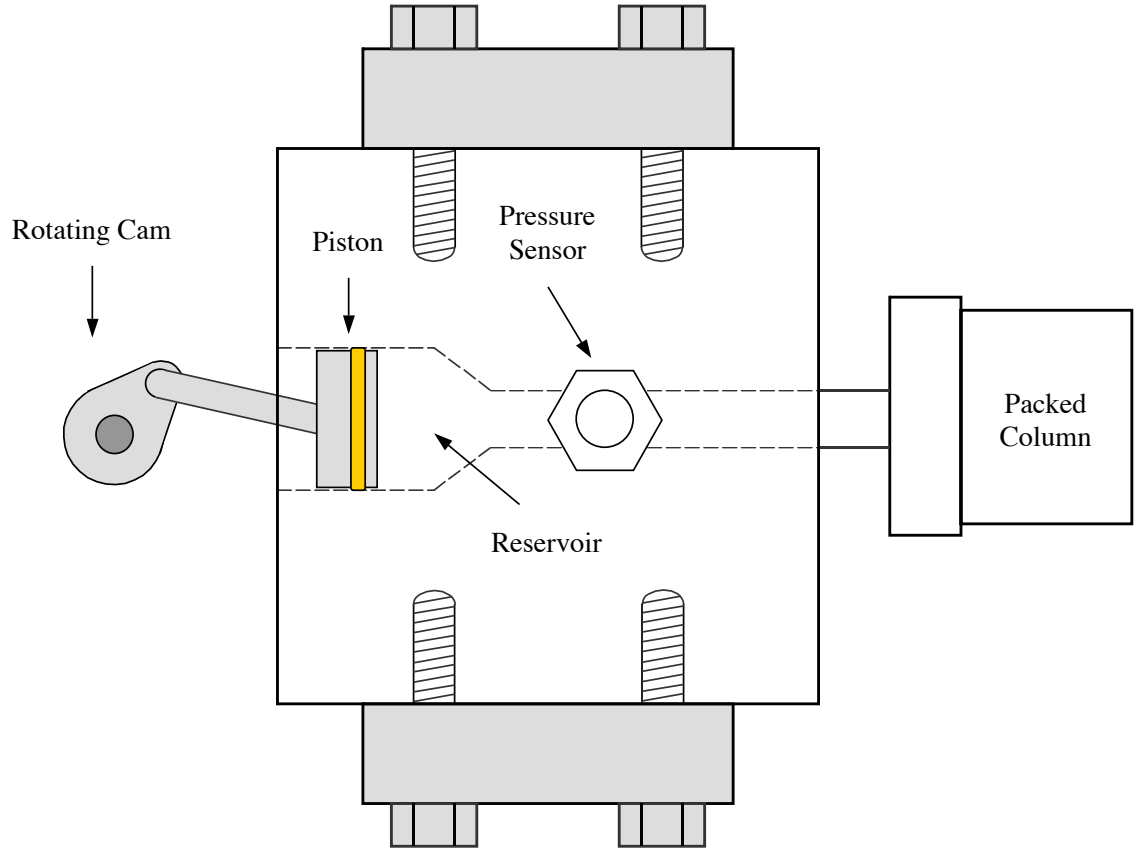

Figure 7.1: A schematic of the new apparatus that will incorporate a rotating cam and a piston that will produce oscillatory flow that whose volume can be directly measured.

7.2 Packed Column Experiments

This study has shown that acoustics increase the transport of colloids with a steady pressure-driven flow. Tatalovich et al., 2000, has shown that humic substances can dramatically increase the dissolution of DNAPLs. Furthermore, Chrysikopoulos and Vogler, 2004, demonstrated that the application of acoustic waves greatly increased the dissolution of various multi-component NAPL mixtures in porous media. The

dissolution enhancement with both colloids and acoustics on DNAPLs will be investigated. First, column experiments will be conducted in 30 cm and 60 cm columns with solutes and various bead sizes to characterize the acoustic properties of the different matrices and to assess attenuation at different frequencies. Then base case colloid experiments will be performed with humic substances or alumina silicate clay particles, both of which are strong sorbents for NAPLs. Finally, experiments will be run with a mass of DNAPL injected in the center of the column and a steady background stream of colloidal particles in the influent. Acoustic waves will then be introduced and the concentrations of aqueous phase and mobile colloid phase DNAPL will be measured and compared.

7.3 New Monolayer Design

Experimental studies have shown that acoustic waves enhance dissolved mass transport of DNAPLs in saturated porous media [*Vogler and Chrysikopoulos*, 2002]. In addition, much work has been done in pore networks and glass bead monolayers on both dissolution and mobilization. The migration of NAPLs in porous media is a function of the NAPL's physicochemical properties and total volume, as well as the aqueous phase saturation, and gravity effects (especially for DNAPLs). It is desirable to be able to investigate at the pore scale, where ganglia-water interfacial areas can be directly observed, the effect of acoustic waves on the dissolution and mobilization of DNAPLs. A monolayer has been constructed to allow for this. A monolayer is essentially a packed bead array consisting of a single layer of glass beads retained between two flat sheets of glass through which water and/or contaminants can flow. The current design allows for viewing from only one side and a horizontal plane orientation such that gravity effects cannot be observed. In addition the area of the packed beads is only approximately 2×5 inches. Figure 7.2 shows the current monolayer array. A new monolayer will be constructed that allows viewing from two directions as well as flow in multiple directions and plane orientations at many dif-

ferent angles. The area of packed beads will be doubled to allow for better viewing. In addition a high resolution camera with macro capabilities and magnifying lenses will allow the capture of digital images on the pore scale. MatLab will be used to process the digital images to obtain good estimations of the surface area, mass, and flux of the DNAPL as experiments are progressing and effluent concentrations are measured.

7.4 Model Aquifer Acoustic Array

The ultimate goal of the previous research would be to create a model in two or three dimensions that will adequately describe the phenomena of acoustically enhanced solute and colloid transport as well as NAPL dissolution and mobilization. Finally a model aquifer (scale to be determined) will be built with a variable array of transducers to test the validity of the model.

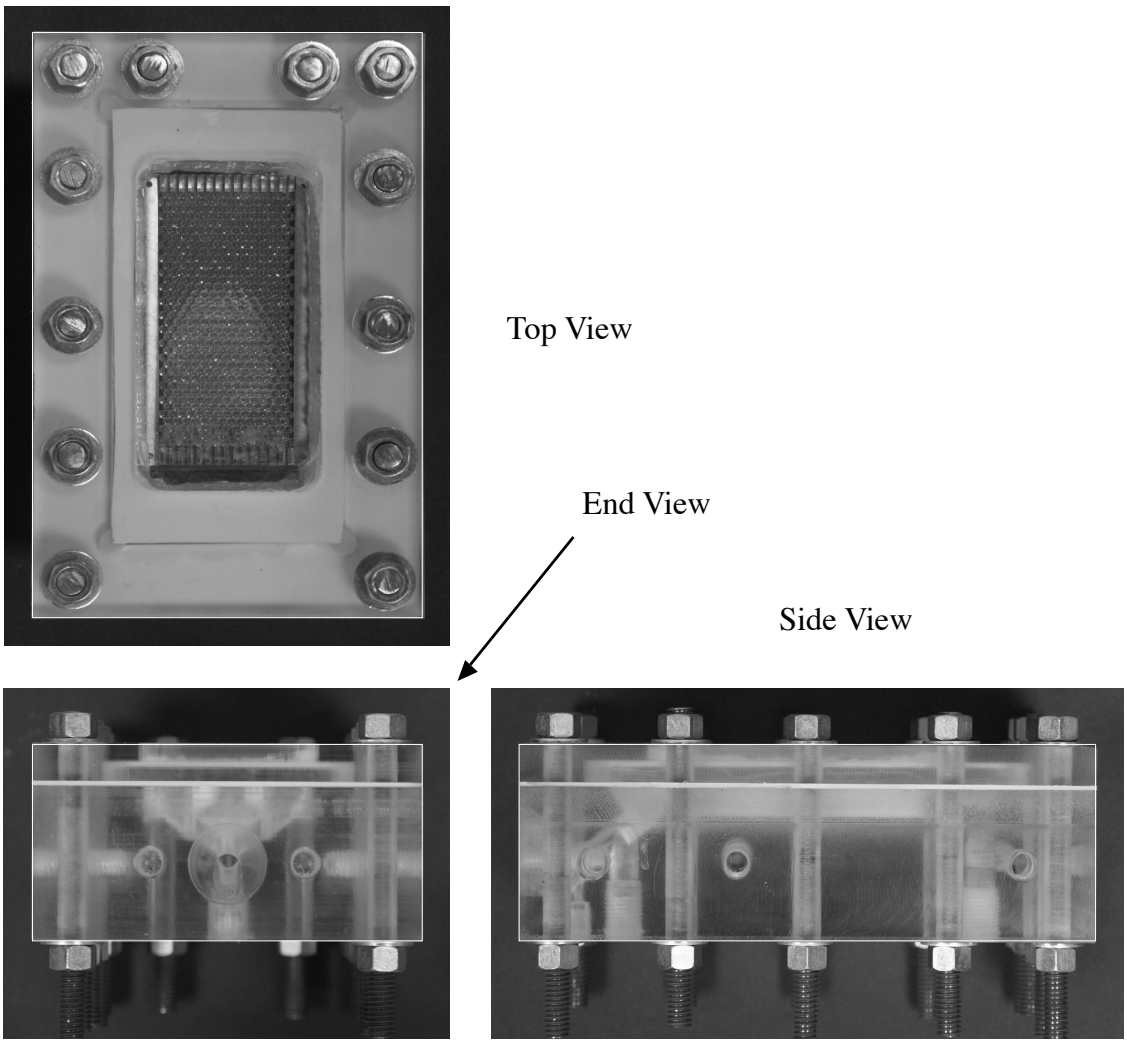

Figure 7.2: The current monolayer design will be modified to allow a larger area of bead packing and the ability to introduce acoustic waves at different angles.

REFERENCES

Abdel-Salam, A. and C. V. Chrysikopoulos, Analytic solutions for one-dimensional colloid transport in saturated fractures, *Adv. Water Resour., 17*, 283-296, 1994.

Abramowitz, M., and I. A. Stegun, eds. *Handbook of Mathematical Functions*, 9th Edition, Dover, Mineola, N. Y., 1972.

Bao, W. M. J., E. T. Vogler, and C. V. Chrysikopoulos, Nonaqueous liquid pool dissolution in three-dimensional heterogeneous subsurface formations, *Environ. Geo., 43*, 968-977, 2003.

Beresnev, I. A. and Johnson, P.A, Elastic-wave stimultaion of oil production: A review of methods and results, *Geophysics, 59*, 1000-1017, 1994.

Biot, M. A., Theory of Propagation of Elastic Waves in a Fluid-Saturated Porous Solid. I. Low-Frequency Range, *J. Appl. Phys., 28*(2), 1956a.

Biot, M. A., Theory of Propagation of Elastic Waves in a Fluid-Saturated Porous Solid. II. Higher Frequency Range, *J. Appl. Phys., 28*(2), 1956b.

Bradford, S. A., K. M. Rathfelder, J. Lang, and L. M. Abriola, Entrapment and dissolution of DNAPLs in heterogeneous porous media, *J. Contam. Hydrol., 67*, 133-157, 2003.

Camesano, T. A., K. M. Unice, and B. E. Logan, Blocking and ripening of colloids in porous media and their implications for bacterial transport, Colloids and Surfaces A: *Physicochem. Eng. Aspects, 160*, 291-308, 1999.

Champ, D. R., and J. Schroeter, Bacterial transport in fractured rock: A field-scale tracer test at the Chalk River Nuclear laboratories, *Water Sci. Technol., 20*, 81-87, 1988.

Chiou, C. T., R. L. Malcolm, T. I. Brinton, and D. E. Kile, Water solubility en-

hancement of some organic pollutants and pesticides by dissolved humic and fulvic acids, *Environ. Sci. Technol. 20*(20), 502-508, 1986.

Chrysikopoulos, C. V., P. K. Kitanidis, and P. V. Roberts, Analysis of one-dimensional solute transport through porous media with spatially variable retardation factor, *Water Resour. Res., 26*(3), 437-446, 1990.

Chrysikopoulos, C. V., P. K. Kitanidis, and P. V. Roberts, Generalized Taylor-Aris moment analysis of the transport of sorbing solutes through porous media with spatially-periodic retardation factor, *Transp. Porous Media, 7*(2), 163-185, 1992.

Chrysikopoulos, C. V., Effective parameters for flow in saturated heterogeneous porous media, J. Hydrol., 170, 181-198, 1995.

Chrysikopoulos, C. V., and Y. Sim, One-dimensional virus transport in homogeneous porous media with time-dependent distribution coefficient, *J. Hydrol., 185*, 199-219, 1996.

Chrysikopoulos, C. V., and A. Abdel-Salam, Modeling colloid transport and deposition in saturated fractures, Colloids and Surfaces A: *Pysicochem. Eng. Aspects, 121*, 189-202, 1997.

Chrysikopoulos, C. V., P. Hsuan, and M. M. Fyrillas, Bootstrap estimation of the mass transfer coefficient of a dissolving nonaqueous phase liquid pool in porous media, *Water Resour. Res., 38*(3), 1-8, 2002.

Chrysikopoulos, C. V., and E. T. Vogler, Acoustically enhanced multicomponent NAPL ganglia dissolution in water saturated packed columns, *Eviron. Sci. Technol., 38*, 2940-2945, 2004.

Corapcioglu, M. Y., and J. Bear eds., Transport Processes in Porous Media, Kluwer Academic Publishers, Boston, 1991.

Corapcioglu, M. Y., and S. Jiang, Colloid-facilitated groundwater contaminant trans-

port, *Water Resour. Res.*, 29, 2215-2226, 1993.

Enfield, C. G., G. Bengtsson, and R. Lindqvist, influence of macromolecules on chemical transport, *Environ. Sci. Technol., 23*, 1278-1286, 1989.

Graham, D. R. and J. J. L. Higdon, Oscillatory forcing of flow through porous media. Part1. Steady flow, *J. Fluid Mech., 456*, 213-235, 2002.

Grindrod, P., The impact of colloids on the migration and dispersal of radionuclides within fractured rock, In: J. I. Kim and G. de Marsily (Editors), Chemistry and migration of actinides and fission products, *J. Contam. Hydrol., 13*, 167-182, 1993.

Grindrod, P., M. S. Edwards, J. J. W. Higgo, and G. M. Williams, Analysis of colloid and tracer breakthrough curves, *J. Contam. Hydrol., 21*, 243-253, 1996.

Gross, A., A. Besov, D. D. Reck, S. Sorek, G. Ben-Dor, A. Britan, and E. Palchikov, Application of Waves for Remediation of Contaminated Aquifers, *Environ. Sci. Technol., 37*, 4481-4486, 2003.

Hiemenz, P. C., and R. Rajagopalan, Principles of Colloid and Surface Chemistry, Third Edition, Marcel Dekker, Inc. New York, 1997.

Higgo, J. J. W., G. M. Williams, I. Harrison, P. Warwick, M. P. Gardiner, and G. Longworh, Colloid transport in a glacial sand aquifer. Laboratory and field studies, *Colloids and Surfaces A, 73*, 179-200, 1993.

Kabala, Z. J., and G. Sposito, A stochastic model of reactive solute transport with time-varying velocity in a heterogeneous aquifer, *Water Resour. Res., 27*(3), 341-350, 1991.

Kretzschmar, R., W.P. Robarge, and A. Amoozegar, Influence of natural organic matter on transport of soil colloids through saprolite, *Water Resour. Res., 31*, 435-445, 1995.

Kretzschmar, R. and H. Sticher, Colloid transport in natural porous media: Influence of surface chemistry and flow velocity, *Phys. Chem. Earth, 23*(2), 133-139, 1998.

Lapidus, L., and N. R. Amundson, Mathematics of adsorption in beds, VI, The effect of longitudinal diffusion in ion exchange and chromatographic columns, *J. Phys. Chem., 56*, 984-988, 1952.

Lenhart, J. J., and J. E. Saiers, Colloid mobilization in water-saturated porous media under transient chemical conditions, *Environ. Sci. Technol., 37*, 2780-2787, 2003.

Loveland, J. P., S. Bhattacharjee, J. N. Ryan, M. Elimelech, Colloid transport in a geochemically heterogeneous porous medium: aquifer tank experiment and modeling, *J. Contam. Hydrol.*, 65, 161-182, 2003.

McCarthy, J. F., Colloid-facilitated transport of contaminants in groundwater: Mobilization of transuranic radionuclides from disposal trenches by natural organic matter, *Phys. Chem. Earth, 23*, 171-178, 1998.

McCarthy, J. F., and F. J. Wobber, eds., Manipulation of Groundwater Colloids for Environmental Restoration, Lewis Publishers, Boca Raton, Florida, 1993.

McCarthy, J. F., and J. M. Zachara, Subsurface transport of contaminants, *Environ. Sci. Technol., 23*, 496-502, 1989.

Mill, W. B., S. Liu, and F. K. Fong, Literature review and model (COMET) for colloid/metals transport in porous media, *Ground Water, 29*, 199-208, 1991.

Niehren, S. and W. Kinzelbach, Artificial collid tracer tests: development of a compact on-line microsphere counter and application to soil column experiments, *J. Contam. Hydrol., 35*, 249-259, 1998.

O'Melia, C. R., M. W. Hahn, and C. T. Chen, Some effects of particle size in separation processes involving colloids, *Water Sci. Technol., 36*, 119-126, 1997.

Reimus, P. W., B. A. Robinson, H. E. Nuttall, and R. Kale, Simultaneous transport of synthetic colloids and a nonsorbing solute through single saturated natural fractures, *Mat. Res. Soc. Symp. Proc., 353*, 363-370, 1995.

Roberts, G. E., and H. Kaufman, *Table of laplace Transforms*, W. B. Saunders, Philadelphia, Pennsylvania, 1966.

Sim, Y., and C. V. Chrysikopoulos, Analytical models for one-dimensional virus transport in saturated porous media, *Water Resour. Res., 31*(5), 1429-1437, 1995. (Correction, *Water Resour. Res., 32*(5), 1473, 1996)

Sirivithayapakorn, S., and A. Keller, Transport of colloids in saturated porous media: A pore-scale observation of the size exclusion effect and colloid acceleration, *Water Resour. Res., 39*, 1-9, 2003.

Smith, P. A., and C. Degueldre, Colloid-facilitated transport of radionuclides through fractured media, *J. Contam. Hydrol., 13*, 143-166, 1993.

Spiegel, M. R., Schaum's ouline of theory and problems of Laplace transforms, McGraw-Hill, New York, 1990.

Stumm, W., Aquatic Colloids As Chemical Reactants: Surface Structure and Reactivity, *Colloids and Surfaces A, 73*, 1-18, 1993.

Tatalovich, M. E., K. Y. Lee, and C. V. Chrysikopoulos, Modeling the transport of Contaminants originating from the dissolution of DNAPL pools in aquifers in the presence of dissolved humic substances, *Trans. Porous Media, 38*, 93-115, 2000.

Tien, N., and S. Li, Transport of a two-member decay chain of radionuclides through a descrete fracture in a porous rock matrix in the presence of colloids, *Nuc. Technol., 140*, 83-93, 2002.

Thomas, A. M. and R. Narayanan, A comparison between the enhanced mass transfer

in boundary and pressure driven oscillatory flow, *Int. J. Heat and Mass Transf., 45*, 4057-4062, 2002.

Valocchi, A. J., Spatial moment analysis of the transport of kinetically adsorbing solutes through stratified aquifers, *Water Resour. Res., 25*(2), 273-279, 1989.

Vogler, E. T., and C. V. Chrysikopoulos, Dissolution of nonaqueous phase liquid pools in anisotropic aquifers, *Stochastic Environ. Res. Risk Assess., 15*, 33-46, 2001.

Vogler, E. T., and C. V. Chrysikopoulos, Experimental investigation of acoustically enhanced solute transport in porous media, *Geophys. Res. Letters, 29*(15), 1-4, 2002.

Vogler, E. T., and C. V. Chrysikopoulos, An experimental study of acoustically enhanced NAPL dissolution in porous media, *AIChE Journal, 50*(12), 3271-3280, 2004.

Weronski, P., J. Y. Walz, and M. Elimelech, Effect of depletion interactions on transport of colloidal particles in porous media, *J. Colloid Int. Sci., 262*, 372-383, 2003.